A study of high-redshift AGN feedback in SZ cluster samples

L. Bîrzan,[1]★ D. A. Rafferty,[1] M. Brüggen[1] and H. T. Intema[2]

[1]*Hamburger Sternwarte, Universität Hamburg, Gojenbergsweg 112, D-21029 Hamburg, Germany*
[2]*Leiden Observatory, Leiden University, Oort Gebouw, PO Box 9513, NL-2300 RA Leiden, the Netherlands*

ABSTRACT

We present a study of active galactic nucleus (AGN) feedback at higher redshifts ($0.3 < z < 1.2$) using Sunyaev–Zel'dovich selected samples of clusters from the South Pole Telescope and Atacama Cosmology Telescope surveys. In contrast to studies of nearby systems, we do not find a separation between cooling flow (CF) clusters and non-CF clusters based on the radio luminosity of the central radio source (cRS). This lack may be due to the increased incidence of galaxy–galaxy mergers at higher redshift that triggers AGN activity. In support of this scenario, we find evidence for evolution in the radio-luminosity function of the cRS, while the lower luminosity sources do not evolve much, the higher luminosity sources show a strong increase in the frequency of their occurrence at higher redshifts. We interpret this evolution as an increase in high-excitation radio galaxies (HERGs) in massive clusters at $z > 0.6$, implying a transition from HERG-mode accretion to lower power low-excitation radio galaxy (LERG)-mode accretion at intermediate redshifts. Additionally, we use local radio-to-jet power scaling relations to estimate feedback power and find that half of the CF systems in our sample probably have enough heating to balance cooling. However, we postulate that the local relations are likely not well suited to predict feedback power in high-luminosity HERGs, as they are derived from samples composed mainly of lower luminosity LERGs.

Key words: galaxies: active – galaxies: clusters: general – galaxies: clusters: intracluster medium – galaxies: elliptical and lenticular, cD – radio continuum: general – X-rays: galaxies: clusters.

1 INTRODUCTION

The co-evolution of galaxies and their supermassive black holes (SMBH) is a key ingredient in our understanding of how the present-day universe came to be. SMBHs interact with (or *feedback* on) their host galaxies via the energetic emission from an active galactic nucleus (AGN), powered by accretion of matter on to the SMBH. A breakthrough in this topic occurred with the discovery that the masses of SMBHs correlate with the properties of their host galaxies, specifically those of the bulge (see the review of Kormendy & Ho 2013). Luminous AGN feedback, in which AGN quench the star formation (SF) in post-starburst galaxies through energetic winds, and the averaging of SMBH masses (inherited in galaxy and SMBH mergers) are natural candidates for the underlying cause of these correlations (Silk & Rees 1998; Fabian, Celotti & Erlund 2006; Fabian 2012; Kormendy & Ho 2013). It is thought that luminous AGN feedback might help to establish these correlations during the wet major-merger stage in galaxy evolution, which makes the classical bulges in low- to moderate-luminosity elliptical galaxies. However, another mode of AGN feedback, in which the AGN output is dominated by mechanical energy, is likely one of the processes that maintains these correlations (Fabian 2012).

In the nearby universe, direct observational evidence for mechanical AGN feedback comes from observations of giant elliptical galaxies, groups and clusters which contain large amounts of hot gas. This discovery was made possible by a new generation of X-ray instruments with high sensitivity and spatial and spectral resolution, namely the *Chandra* and *XMM–Newton* observatories. Data from these instruments showed X-ray cavities or bubbles filled with radio emission, which include notable examples as Perseus (Fabian et al. 2000), Hydra A (McNamara et al. 2000), A2052 (Blanton et al. 2001), M87 (Forman et al. 2005), MS0735+74 (McNamara et al. 2005) among many others (Bîrzan et al. 2004; Dunn & Fabian 2004; Rafferty et al. 2006; Bîrzan et al. 2012). Additionally, these data show a lack of spectroscopic evidence for gas cooling below 2 keV (Peterson et al. 2001).

The existence of such feedback alleviates a long-standing problem in cluster studies known as the cooling flow (CF) problem (Fabian 1994). In the initially proposed scenario by Fabian (1994), the gas is heated up to 10^7 K by the initial gravitational collapse when clusters form. In the centre of clusters, where the density is high and the temperature is low, the cooling time can be less than the *Hubble* time ($t_{cool} < t_H$). In this case, it was postulated

★E-mail: lbirzan@hs.uni-hamburg.de

that a 'CF' should form, in which gas cools and flows inward in quasi-hydrostatic equilibrium. However, searches for the high-mass deposition rates predicted by this model have found that cooling seems to be proceeding at much lower rates than predicted (e.g. Peterson et al. 2001). Instead of steady cooling throughout the core, it appears that cooling occurs primarily as a result of local cooling instabilities, regulated by feedback (e.g. Voit et al. 2016).

Studies of samples of systems with X-ray cavities found a strong correlation between the mechanical power injected into the hot gas by the AGN through cavities (i.e. the $4pV$ enthalpy of the buoyantly rising cavities) and the cooling rates of this gas (Bîrzan et al. 2004; Dunn & Fabian 2004; Rafferty et al. 2006). From this evidence, it was postulated that the AGN are heating the gas and regulating cooling through a feedback loop. This process is known as the *jet-mode*, *maintenance-mode*, or *radio-mode* AGN feedback and is commonly observed in the nearby universe, where no significant brightest cluster galaxy (BCG) growth typically occurs. In jet-mode AGN feedback, the accretion rate is thought to be well below the Eddington limit, with the bulk of the energy released in kinetic form by two-sided radio-bright jets. Galaxies with such AGN tend to be low-excitation radio galaxies (LERGs), based on the presence of weak, narrow, low-ionization emission lines (Hine & Longair 1979; Hardcastle, Evans & Croston 2006, 2007; Best & Heckman 2012). LERGs may be powered by hot-mode accretion, when the material falls directly on to the SMBH through accretion of clumps of gas (known as the *cold feedback mechanism*, Pizzolato & Soker 2005; Soker 2006; Pizzolato & Soker 2010; Gaspari, Ruszkowski & Sharma 2012; Gaspari, Brighenti & Temi 2015; McCourt et al. 2012; Sharma et al. 2012; Li et al. 2015; Prasad, Sharma & Babul 2015; Voit et al. 2015, 2016), with no accretion disc to ionize (see also observational support from Rafferty, McNamara & Nulsen 2008; Cavagnolo et al. 2011; Farage, McGregor & Dopita 2012; McNamara et al. 2014).

SF is an important ingredient in the feedback process because, as the gas cools down, some of it should to go to fuel SF (through residual cooling). There are several pieces of evidence for this residual cooling, such as the observed correlation between the observed star formation rates (SFRs) and the residual cooling rates (McNamara & O'Connell 1989; Koekemoer et al. 1999; McNamara, Wise & Murray 2004; Rafferty et al. 2008; O'Dea et al. 2008; Donahue et al. 2010; Hicks, Mushotzky & Donahue 2010; McDonald et al. 2011; Oonk et al. 2011; Donahue et al. 2015; Fogarty et al. 2015; Mittal, Whelan & Combes 2015; Tremblay et al. 2015, 2016). Cooling should occur when the central cooling time (or entropy, or the ratio of cooling to dynamical time) becomes low enough that thermally unstable condensing clouds form from the hot atmosphere (Rafferty et al. 2008; Voit et al. 2008; Sharma et al. 2012; Gaspari et al. 2012; Voit & Donahue 2015; Voit et al. 2015; Guo & Mathews 2014; Brighenti, Mathews & Temi 2015; Valentini & Brighenti 2015; Prasad et al. 2015). X-ray cavities likely have an important role in uplifting some of the cooling gas from the cluster centre (Simionescu et al. 2008; Werner et al. 2010, 2011; Kirkpatrick, McNamara & Cavagnolo 2011; Vantyghem et al. 2016; Russell et al. 2016), and there is evidence that the soft X-ray gas cools and forms Hα emission and cold molecular clouds in a filamentary structure (McDonald et al. 2010; Werner et al. 2014; Tremblay et al. 2015; McNamara et al. 2014, 2016; Fabian et al. 2016).

The feedback process is expected to operate in CFs. The cooling time in the core is a basic selection criterion for the cooling systems: if the central cooling time of a system is smaller than its age, which is typically a significant fraction of the *Hubble* time, then one expects that this system needs heating to prevent cooling (see

Bîrzan et al. 2012; Panagoulia, Fabian & Sanders 2014a; Panagoulia et al. 2014b). Additionally, as mentioned above, the ratio of cooling time to free-fall time has proved to be a sensitive indicator of the presence of cooling, both in observations and simulations (e.g. Voit et al. 2008; Bîrzan et al. 2012; Sharma et al. 2012; Li et al. 2015).

However, many of the details of AGN feedback are missing from this picture or are poorly understood (e.g. how the energy is transported to cluster scales, either through weak shocks, turbulence, mixing, sound waves or cosmic rays; Zhuravleva et al. 2014, 2016; Banerjee & Sharma 2014; Wagh, Sharma & McCourt 2014; Hillel & Soker 2014, 2017; Yang & Reynolds 2016; Fabian et al. 2017; Tang & Churazov 2017; Pfrommer 2013; Ruszkowski, Yang & Reynolds 2017). Additionally, there are few direct studies of feedback in clusters at high redshifts ($z > 0.5$).

1.1 AGN feedback at higher redshifts

The question of how much heating is produced by AGN at higher redshifts is important since it is at these redshifts that the bulk of galaxy and cluster formation occurred and, consequently, that the effects of AGN feedback were likely most instrumental in shaping them. On the cooling side, there is evidence of evolution in the cuspiness of the density profile (Donahue, Stocke & Gioia 1992; Vikhlinin et al. 2007; Santos et al. 2010; Samuele et al. 2011; McDonald et al. 2011, 2013b) since $z \sim 1$. However, recent results from the SPT–SZ survey (Carlstrom et al. 2011; Bleem et al. 2015) do not find evidence of evolution in the cooling properties of the intracluster medium (ICM) in the redshift range $0.3 < z < 1.2$, only in the cuspiness (McDonald et al. 2017).

On the heating side, there is little evidence for evolution in jet-mode AGN feedback in the general population of radio-loud (RL) AGN using deep-field surveys up to $z \sim 1.3$, suggesting that jet-mode feedback starts to operate as early as 7 Gyr after big bang and does not change since (e.g. Simpson et al. 2013), thus maintaining the same approximate balance between AGN heating and radiative cooling as in the local universe (Best et al. 2006). The only direct study of jet-mode feedback in higher redshift systems was done by Hlavacek-Larrondo et al. (2012) using the MAssive Cluster Survey (MACS) sample and reached only to redshifts of $z \sim 0.5$. Other studies of AGN feedback at high redshift (Lehmer et al. 2007; Smolčić et al. 2009; Danielson et al. 2012; Ma, McNamara & Nulsen 2013; Best et al. 2014) rely on indirect methods of inferring AGN feedback powers, such as scaling relations between the jet (mechanical) power and the radio luminosity (Bîrzan et al. 2004, 2008; Cavagnolo et al. 2010; O'Sullivan et al. 2011; Daly et al. 2012; Antognini, Bird & Martini 2012; Godfrey & Shabala 2013).

Until recently, the majority of complete cluster samples were X-ray flux-limited samples, e.g. the B55 (Edge et al. 1990), HI-FLUGCS (Reiprich & Böhringer 2002), and REFLEX (Böhringer et al. 2004) samples. However, recently a number of Sunyaev–Zel'dovich (SZ) surveys have been undertaken, such as the Atacama Cosmology Telescope (ACT; Fowler et al. 2007; Marriage et al. 2011; Hasselfield et al. 2013), South Pole Telescope (SPT; Carlstrom et al. 2011; Reichardt et al. 2013; Bleem et al. 2015), and *Planck* (Planck Collaboration XXIX 2014) surveys. The main advantages of SZ surveys is that the SZ signal is independent of redshift (Song et al. 2012; Reichardt et al. 2013) and is closely related to the cluster mass with very little scatter (Motl et al. 2005). Consequently, these surveys have identified the most massive clusters up to and beyond redshifts of ~ 1, and thus are important for understanding the high-redshift universe.

For AGN feedback studies, such a sample allows for comparisons of feedback properties among samples with different selection

criteria (i.e. mass versus X-ray flux), allowing us to identify potential biases. For example, it is known that at higher redshift (above 0.5) ∼50 per cent of radio-loud quasars (RLQs), and other powerful radio galaxies, are located in rich clusters of galaxies (Yee & Green 1987; Yates, Miller & Peacock 1989; Hall & Green 1998; Hill & Lilly 1991). These powerful sources may obscure the thermal signature of the ICM and result in incomplete X-ray flux-limited cluster samples.

In this paper, we use the SPT and ACT SZ cluster samples to study AGN feedback at $z > 0.3$. These samples are well studied at a variety of wavelengths and have extensive archival *Chandra* data, making them ideally suited to our purposes. In addition to archival *Chandra* data, we use radio data from Sydney University Molonglo Sky Survey (SUMSS) and NRAO VLA Sky Survey (NVSS, plus targeted GMRT observations for a small subsample) and SFRs from McDonald et al. (2016). We assume $H_0 = 70$ km s^{-1} Mpc^{-1}, $\Omega_\Lambda = 0.7$, and $\Omega_M = 0.3$ throughout.

2 SAMPLE

Our sample consists of 99 systems with archival *Chandra* data from the SZ surveys of the southern and equatorial sky (SPT and ACT; Carlstrom et al. 2011; Fowler et al. 2007). The SPT survey covers an area of 2500 deg^2, with 677 cluster candidates above a signal-to-noise threshold of 4.5 (Ruel et al. 2014; Bleem et al. 2015), which represents a mass-limited sample (∼80 per cent complete at $M > 5 \times 10^{14}$ M$_\odot$) to arbitrarily large distances. From this sample, the 80 cluster candidates with the highest SZ-effect detection significance have been observed with *Chandra*, through a *Chandra* X-ray Visionary Project (PI: Benson) or other GO/GTO programmes (e.g. PI: Mohr, Romer), resulting in ∼ 2000 counts per system. To this sample of 80 clusters, we added a number of other SPT systems which have archival *Chandra* data (e.g. RDCS J0542−4100, PI: Ebeling; RXC J0232.2−4420, PI: Böhringer). We did not include SPT-CL J0330−5228 ($z = 0.44$), since the clusters A3125/A3128 ($z = 0.06$) are in the foreground, and SPT-CL J0037−5047 ($z = 1.026$) because of insufficient counts in the X-ray data.

The ACT SZ survey is a sample of 91 systems (∼90 per cent complete at $M > 5 \times 10^{14}$ M$_\odot$) from within a nearly 1000 deg^2 area (Hasselfield et al. 2013), identified during the 2008 (southern survey; Marriage et al. 2011), 2009 and 2010 (equatorial survey; Hasselfield et al. 2013) campaigns. Of these, 18 clusters with the most significant SZ-effect detections were observed with *Chandra* (PI: Hughes). As with the SPT clusters, the exposure times were such as to obtain ∼2000 counts per system (or a minimum of 20–30 ks). In addition to these systems, we added four extra ACT clusters that had *Chandra* observations: ACT-CL J0326−0043 (MACS J0326−0043; PI: Ebeling), ACT-CL J0152−0100 (A267; PI: Vanspeybroeck), ACT-CL J2337−0016 (A2631; PI: Bonamente), and ACT-CL J2129−0005 (RXC J2129.6+0005; PI: Allen).

We note that recent simulations (Lin et al. 2015) have shown that SZ observations can be biased by the presence of a cool core and a RL AGN, in the sense that a cool core increases the SZ signal and an RL AGN decreases it. However, such biases are expected to be small overall in SZ samples (Lin et al. 2015; Gupta et al. 2016).

In summary, we have constructed a sample of 99 massive southern and equatorial clusters with ∼2000 X-ray counts per system. These data allow us to obtain reliable temperature and pressure profiles (see also McDonald et al. 2013b) to achieve our goal of understanding the state of the system, such as its cooling time (see Section 3), and, along with complementary radio data, the impact of AGN feedback.

3 DATA ANALYSIS

3.1 X-ray analysis

All systems were observed with the *Chandra* ACIS detector in imaging mode, and the X-ray data were obtained from the *Chandra* Data Archive. Details of the observations are given in Table 1.

The *Chandra* data were reprocessed with CIAO 4.8 using CALDB 4.7.2 and were corrected for known time-dependent gain and charge transfer inefficiency problems. Blank-sky background files, normalized to the count rate of the source image in the 10–12 keV band, were used for background subtraction.[1]

Analysis of the X-ray data closely followed that of Rafferty et al. (2008) and Bîrzan et al. (2012). However, in contrast to these works, where 2000 counts per spectrum were commonly used, in this sample we have only 2000 counts in total for a majority of the systems. As a result, to obtain spectra at least two radii, the X-ray spectra were extracted in circular annuli with as low as ∼750 counts centred on the centroid of the cluster emission. The lower number of counts results in larger errors on the derived quantities, but not so large that they are not useful in assessing the state of the system. A majority of the systems have at least three radial bins, except for 10 systems, marked in Table 1 (in the kT column), which have two bins only. In some systems, due to the diffuse nature of the cluster emission or to substructure, the centroid of the X-ray emission was difficult to identify precisely. These systems are noted in Table 1 (in the X-ray-core column). Spectra and their associated weighted responses were made for the annuli using CIAO and were fit in XSPEC version 12.5.1.

Gas temperatures and densities (listed in Table 1) were found by deprojecting the spectra with a single-temperature plasma model (MEKAL) with a foreground absorption model (WABS) using the PROJECT mixing model. In this fit, we fixed the redshift to those listed in Table 2, the hydrogen column density to the value of Dickey & Lockman (1990) at the cluster position, and the abundance of the MEKAL component to be at least 0.3 times the solar abundance (see Mernier et al. 2017). Our central values are typically within a factor of two of the central values reported by McDonald et al. (2013b), with larger discrepancies attributable to differences in the annuli and deprojection techniques between our study and theirs.

We derived the cooling times using the deprojected densities and temperatures found above and the cooling curves of Smith et al. (2001). The pressure in each annulus was calculated as $p = nkT$, where we have assumed an ideal gas and $n = 2n_e$. To derive densities as close to the core as possible, we used the onion-peel deprojection method described in Rafferty et al. (2008). This method assumes that changes in the surface brightness (SB) within this region are dominated by changes in the density. Therefore, the temperature and abundance of the gas are assumed to be constant in the inner region used in spectral deprojection. We then extrapolated the density profile inward using the SB profile, accounting for projection effects under the assumption of spherical symmetry. The SB profiles were derived in annuli with a width of 10 pixels (≈4″9), with typical annulus containing ∼100 counts.

Within the cooling radius, radiative energy losses must be replaced to prevent the deposition of large quantities of cool gas. Therefore, to assess whether a system has enough energy to balance cooling, ones needs the luminosity of the cooling gas inside the cooling radius. To be consistent with previous works (e.g.

[1] See http://asc.harvard.edu/contrib/maxim/acisbg/.

Table 1. X-ray properties.

System[a]	Obs. ID[b]	t[c] (ks)	X-ray core (J2000)[d] RA	Dec.	kT[e] (keV)	n_e[f] (cm^{-3})	r[g] (kpc)	$\Delta(kT)$[h]	t_{cool}[i] (Gyr)	t_{cool} (10 kpc)[j] (Gyr)	$\frac{t_{cool}}{t_{ff}}$[k]	η_{min}[l]
SPT-CL J0000−5748	9335	29.6	00 00 59.97	−57 48 33.66	$5.46^{+1.46}_{-0.96}$	$0.040^{+0.002}_{-0.002}$	24.6	$1.65^{+1.22}_{-0.74}$	$1.08^{+0.40}_{-0.29}$	$0.44^{+0.60}_{-0.12}$	7.92	5.40
SPT-CL J0013−4906	13462	11.5	00 13 19.65	−49 06 38.11	$5.63^{+4.12}_{-1.93}$	$0.0056^{+0.0004}_{-0.0002}$	72.0	–	$9.27^{+4.11}_{-3.31}$	$1.12^{+0.51}_{-0.41}$	16.41	20.03
ACT-CL J0014−0056	16228	28.3	00 14 54.47*	−00 57 04.9*	$5.96^{+2.88}_{-1.61}$	$0.013^{+0.001}_{-0.001}$	43.5	$1.88^{+1.35}_{-1.05}$	$3.96^{+1.67}_{-1.45}$	$1.85^{+0.81}_{-0.71}$	16.45	24.36
SPT-CL J0014−4952	13471	46.5	00 14 50.1*	−49 52 54.24*	$7.90^{+4.23}_{-2.52}$*	$0.037^{+0.001}_{-0.001}$	83.1	–	$10.96^{+6.30}_{-4.47}$	$3.19^{+2.02}_{-1.56}$	23.83	125.68
ACT-CL J0022−0036	16226	53.5	00 22 13.35	−00 36 35.13	$10.55^{+10.14}_{-3.87}$	$0.0069^{+0.0005}_{-0.0005}$	66.6	–	$9.69^{+6.78}_{-3.67}$	$3.73^{+2.67}_{-1.51}$	26.22	190.34
SPT-CL J0033−6326	13483	17.8	00 33 52.68*	−63 26 39.84*	$3.89^{+1.63}_{-0.62}$	$0.0069^{+0.0011}_{-0.0017}$	67.3	$2.67^{+2.57}_{-1.49}$	$3.90^{+5.27}_{-2.60}$	$1.60^{+2.22}_{-1.17}$	10.45	6.68
SPT-CL J0040−4407	13395	6.4	00 40 50.59*	−44 07 52.44*	$10.8^{+13.3}_{-3.4}$*	$0.0092^{+0.0001}_{-0.0001}$	60.7	–	$6.87^{+5.27}_{-2.75}$	$3.26^{+2.29}_{-1.63}$	20.42	128.20
SPT-CL J0058−6145	13479	44.6	00.58 20.9	−61 46 01.8	$9.96^{+14.02}_{-4.52}$	$0.0057^{+0.0005}_{-0.0004}$	63.6	–	$12.27^{+9.03}_{-4.83}$	$2.00^{+1.48}_{-0.81}$	34.88	275.44
ACT-CL J0059−0049	16227	36.6	00 59 08.86*	−00 50 06.18	$7.90^{+3.25}_{-2.08}$	$0.0063^{+0.0001}_{-0.0001}$	82.6	$2.94^{+2.42}_{-1.62}$	$9.50^{+2.07}_{-2.34}$	$3.50^{+1.13}_{-1.20}$	20.78	64.51
SPT-CL J0102−4603	13485	54.1	01:02:42.5*	−46:04:19.6*	$3.044^{+1.18}_{-0.89}$	$0.0046^{+0.0006}_{-0.0005}$	69.3	$1.50^{+0.95}_{-0.84}$	$8.19^{+2.76}_{-3.62}$	$3.40^{+1.54}_{-1.82}$	21.34	10.23
ACT-CL J0102−4915*	14022	145.9	01 02 58.078*	−49 16 29.23*	$3.55^{+0.60}_{-0.40}$	$0.067^{+0.004}_{-0.004}$	15.2	$4.08^{+1.09}_{-1.13}$	$0.461^{+0.150}_{-0.120}$	$0.480^{+0.158}_{-0.127}$	5.76	1.39
SPT-CL J0106−5943	13468	16.1	01:06:28.19	−59:43:12.5	$7.60^{+5.56}_{-1.94}$	$0.0079^{+0.0006}_{-0.0006}$	47.2	–	$6.834^{+4.50}_{-2.24}$	$3.94^{+3.06}_{-2.08}$	26.17	103.80
SPT-CL J0123−4821	13491	59.9	01:23:12.054	−48:21:25.25	$8.79^{+6.49}_{-2.98}$	$0.0037^{+0.0002}_{-0.0002}$	76.8	–	$17.79^{+10.61}_{-4.30}$	$10.11^{+8.73}_{-6.75}$	41.68	305.70
SPT-CL J0142−5032	13467	23.3	01:42:10.63*	−50:32:23.28*	$8.20^{+8.18}_{-3.63}$	$0.0050^{+0.0002}_{-0.0005}$	82.2	–	$12.16^{+8.24}_{-5.55}$	$3.73^{+2.93}_{-2.26}$	26.74	114.28
SPT-CL J0151−5954	13480,14380	46.1,29.4	01:51:26.9*	−59:54:29.4*	$3.79^{+1.38}_{-0.77}$	$0.0019^{+0.0004}_{-0.0003}$	54.6	–	$15.84^{+14.79}_{-8.36}$	$7.62^{+8.66}_{-6.37}$	52.46	130.48
ACT-CL J0152−0100*	3580	17.7	01 52 42.5*	01 00 42.8*	$7.96^{+8.84}_{-3.23}$	$0.010^{+0.001}_{-0.001}$	27	–	$5.57^{+4.37}_{-2.29}$	$4.42^{+4.31}_{-3.14}$	37.1	234.2
SPT-CL J0156−5541	13489	68.1	01:56:10.55*	−55:41:54*	$11.56^{+18.82}_{-5.44}$	$0.0079^{+0.0009}_{-0.0007}$	55.2	–	$9.66^{+8.26}_{-4.58}$	$2.65^{+2.28}_{-1.29}$	31.63	301.84
SPT-CL J0200−4852	13487	20.7	02:00:34.9*	−48:52:10.8*	$7.84^{+13.29}_{-3.14}$	$0.0057^{+0.0006}_{-0.0005}$	56.9	$1.73^{+1.80}_{-3.02}$	$8.86^{+11.22}_{-4.09}$	–	28.13	136.68
ACT-CL J0206−0114	16229	26.9	02 06 13.64*	−01 15 13.37*	$5.83^{+1.98}_{-1.32}$	$0.0043^{+0.0003}_{-0.0002}$	110.9	$2.85^{+2.53}_{-1.60}$	$12.44^{+5.11}_{-2.19}$	$2.71^{+1.18}_{-0.61}$	20.26	32.53
ACT-CL J0212−4656	13464	25.2	02:12:23.6*	−46:57:15.1*	$4.86^{+3.14}_{-1.33}$	$0.0032^{+0.0002}_{-0.0005}$	82.1	–	$11.18^{+10.75}_{-5.30}$	$1.50^{+1.45}_{-0.74}$	24.60	44.18
ACT-CL J0215−5212	12268	16.9	02 15 11.86*	−52 12 21.51*	$5.85^{+2.23}_{-1.20}$*	$0.0020^{+0.0001}_{-0.0001}$	160.1	–	$23.33^{+8.62}_{-5.73}$	$6.28^{+3.45}_{-2.98}$	25.49	56.76
ACT-CL J0217−5245	12269	18.0	02 17 15.05*	−52 45 43.82*	$7.56^{+6.29}_{-2.16}$	$0.0016^{+0.0000}_{-0.0000}$	114.4	–	$29.13^{+23.03}_{-10.68}$	–	46.0	359.73
SPT-CL J0232−4420*	4993	11.1	02 32 18.65	−44 20 47.37	$4.97^{+0.87}_{-0.64}$	$0.039^{+0.002}_{-0.002}$	29.5	$1.86^{+0.41}_{-0.40}$	$0.99^{+0.29}_{-0.23}$	$0.83^{+0.26}_{-0.21}$	8.89	6.02
ACT-CL J0232−5257	12263	18.0	02 32 48.81*	−52 57 12.84*	$7.03^{+2.96}_{-1.93}$	$0.0024^{+0.0002}_{-0.0001}$	147.4	$2.13^{+1.06}_{-0.65}$	$24.15^{+6.65}_{-6.89}$	–	28.76	93.52
SPT-CL J0234−5831	13403	9.2	02 34 41.93	−58 31 24.11	$4.60^{+1.71}_{-1.03}$	$0.012^{+0.001}_{-0.001}$	28.4	$4.15^{+3.26}_{-3.86}$	$1.38^{+0.47}_{-0.46}$	$0.912^{+0.317}_{-0.318}$	8.76	4.13
ACT-CL J0235−5121	12262	17.5	02 35 44.61*	−51 20 59.18*	$5.11^{+1.97}_{-1.18}$	$0.0035^{+0.0002}_{-0.0002}$	57.1	$1.36^{+0.44}_{-0.57}$	$11.06^{+4.95}_{-3.23}$	–	26.32	54.09
ACT-CL J0237−4939	12266	36.5	02 37 01.46	−49 38 09.37	$5.90^{+1.49}_{-1.27}$	$0.0037^{+0.0001}_{-0.0001}$	57.7	–	$14.26^{+4.78}_{-2.42}$	$5.22^{+2.09}_{-1.44}$	39.80	128.30
SPT-CL J0243−5930	13484,15573	23.5,16.5	02 43 27.109*	−59 31 03.02*	$7.24^{+5.35}_{-1.03}$	$0.012^{+0.0005}_{-0.0008}$	42.6	$1.43^{+0.86}_{-0.73}$	$5.00^{+2.56}_{-1.65}$	$3.23^{+1.92}_{-1.45}$	15	56.83
ACT-CL J0245−5302*	12260	18.4	02 45 24.734	−53 01 45.9	$7.20^{+49.46}_{-4.23}$	$0.0057^{+0.0000}_{-0.0000}$	37.2	$2.13^{+1.06}_{-0.65}$	$9.11^{+23.70}_{-8.64}$	$2.45^{+6.38}_{-2.35}$	44.20	265.66
SPT-CL J0252−4824	13494	25.8	02:52:48.38	−48:24:44.53	$2.90^{+3.95}_{-1.32}$	$0.0032^{+0.0010}_{-0.0006}$	60.0	$2.45^{+1.55}_{-3.40}$	$11.36^{+10.25}_{-7.83}$	$3.23^{+2.98}_{-2.32}$	34.23	23.79
SPT-CL J0256−5617	13481,14448	19.0,22.5	02 56 26.23*	−56 17 49.11*	$6.92^{+38.48}_{-3.05}$	$0.0030^{+0.0000}_{-0.0000}$	86.3	–	$11.33^{+36.41}_{-8.18}$	–	23.71	106.05
SPT-CL J0304−4401	13402	12.8	03 04 16.608	−44 01 31.94	$6.23^{+4.01}_{-2.07}$*	$0.0034^{+0.0000}_{-0.0000}$	98.7	$1.53^{+0.90}_{-1.06}$	$11.51^{+7.31}_{-4.89}$	$3.38^{+2.29}_{-1.62}$	21.06	56.19
ACT-CL J0304−4921	12265	18.2	03 04 16.24	−49 21 25.2	$4.15^{+1.16}_{-0.73}$	$0.019^{+0.002}_{-0.002}$	27.4	$1.86^{+0.89}_{-0.68}$	$1.64^{+0.87}_{-0.61}$	$0.91^{+0.48}_{-0.34}$	9.73	5.73
SPT-CL J0307−5042	13476	33.3	03 07 50.87	−50 42 07.68	$4.36^{+1.20}_{-1.20}$	$0.0060^{+0.0007}_{-0.0007}$	64.7	$2.94^{+2.16}_{-1.97}$	$6.51^{+4.28}_{-2.99}$	$4.24^{+3.49}_{-2.87}$	18.19	17.32
SPT-CL J0307−6225	12191	21.1	03 07 15.6	−62 26 50.7	$3.34^{+1.26}_{-0.69}$	$0.0012^{+0.0004}_{-0.0004}$	176.2	$2.26^{+1.60}_{-1.23}$	$154.19^{+287.58}_{-122.33}$	$1.90^{+3.57}_{-1.57}$	15.81	13.81

Table 1 – *continued*

System[a]	Obs. ID[b]	t[c] (ks)	X-ray core (J2000)[d] RA	Dec.	kT[e] (keV)	n_e[f] (cm^{-3})	r[g] (kpc)	$\Delta(kT)$[h]	t_{cool}[i] (Gyr)	t_{cool} (10 kpc)[j] (Gyr)	$\frac{t_{cool}}{t_{ff}}$[k]	η_{min}[l]
SPT-CL J0310−4646	13492	32.3	03 10 32.3*	−46 47 08.7*	$6.56^{+2.36}_{-1.65}$	$0.0052^{+0.0004}_{-0.0003}$	90.1	$1.14^{+3.42}_{-1.17}$	$10.026^{+3.35}_{-2.83}$	−	20.11	43.55
SPT-CL J0324−6236	12181,13137 13213	18.5,21.6 10.9	03 24 12.48	−62 35 57.18	$8.85^{+2.71}_{-2.04}$	$0.0075^{+0.0003}_{-0.0003}$	69.3	−	$87.95^{+18.37}_{-19.61}$	$5.78^{+3.11}_{-3.15}$	22.93	94.74
...												
ACT-CL J0326−0043*	5810	9.4	03 26 49.9	−00 43 51.9	$3.91^{+1.19}_{-0.85}$	$0.138^{+0.10}_{-0.008}$	11.3	$1.79^{+0.53}_{-0.61}$	$0.28^{+0.10}_{-0.03}$	$0.256^{+0.090}_{-0.025}$	3.51	0.66
SPT-CL J0334−4659	13470	22.7	03 34 11.03	−46 59 45.6	$4.61^{+0.95}_{-0.48}$	$0.020^{+0.001}_{-0.001}$	34.0	$1.25^{+0.36}_{-0.34}$	$2.31^{+0.46}_{-0.46}$	$0.83^{+0.17}_{-0.18}$	10	8.01
ACT-CL J0346−5438	12270,13155	17.3,15.2	03 46 56	−54 38 54.09	$6.35^{+2.43}_{-1.42}$	$0.0042^{+0.0002}_{-0.0002}$	94.4	−	$11.92^{+4.34}_{-3.01}$	−	22.40	51.70
SPT-CL J0348−4514	13465	12.3	03 48 16.9*	−45 15 05.13*	$3.33^{+1.09}_{-0.70}$	$0.0041^{+0.0003}_{-0.0005}$	92.5	$3.66^{+3.74}_{-1.75}$	$9.51^{+3.04}_{-3.24}$	−	18.51	9.25
SPT-CL J0352−5647	13490	30.4	03 52 57.8	−56 47 50.3	$5.70^{+2.51}_{-1.22}$	$0.0033^{+0.0000}_{-0.0000}$	109.8	−	$11.68^{+5.14}_{-3.16}$	$3.92^{+2.33}_{-1.90}$	19.22	38.03
SPT-CL J0406−4804	13477	22.7	04 06 55.7*	−48 04 47.75*	$7.60^{+3.72}_{-1.96}$	$0.0025^{+0.0001}_{-0.0001}$	168.5	−	$23.14^{+8.93}_{-6.39}$	$3.08^{+1.30}_{-1.00}$	24.80	89.13
SPT-CL J0411−4819	16355,17536	24.4,31.0	04 11 16.181	−48 18 55.47	$5.44^{+1.21}_{-1.15}$	$0.0150^{+0.0008}_{-0.0007}$	31.5	$1.85^{+1.06}_{-1.04}$	$3.39^{+0.57}_{-0.75}$	$1.86^{+0.35}_{-0.44}$	19.44	26.70
SPT-CL J0417−4748	13397	20.2	04 17 23.49	−47 48 49.939	$4.53^{+0.75}_{-0.56}$	$0.026^{+0.001}_{-0.001}$	37.3	$2.70^{+0.83}_{-0.97}$	$1.45^{+0.35}_{-0.30}$	$0.90^{+0.24}_{-0.21}$	7.02	2.99
SPT-CL J0426−5455	13472	28.3	04 26 05.32	−54 54 57.16	$10.37^{+6.88}_{-5.47}$	$0.0022^{+0.0000}_{-0.0000}$	140.2	−	$31.83^{+10.77}_{-17.42}$	−	41.02	424.77
ACT-CL J0438−5419	12259	18.1	04 38 17.32	−54 19 23.06	$9.22^{+3.28}_{-2.11}$	$0.0150^{+0.0008}_{-0.0008}$	42.2	$1.33^{+0.74}_{-0.42}$	$3.86^{+1.54}_{-1.05}$	$2.19^{+0.94}_{-0.69}$	10	15
SPT-CL J0441−4854	13475	22.2	04 41 48.38*	−48 55 26.8*	$6.60^{+3.75*}_{-1.83}$	$0.0132^{+0.0000}_{-0.0000}$	49.7	$1.09^{+0.58}_{-0.67}$	$4.03^{+1.77}_{-1.26}$	$2.67^{+1.37}_{-1.10}$	14.68	23.50
SPT-CL J0446−5849	13482,15560	28.3,18.6	04 46 04.7*	−58 49 55.5*	$5.77^{+2.88*}_{-1.93}$	$0.0025^{+0.001}_{-0.001}$	179.3	−	$19.74^{+5.54}_{-7.56}$	$3.95^{+2.52}_{-1.59}$	19.97	32.62
SPT-CL J0449−4901	13473	42.8	04 49 06.26*	−49 01 36.42*	$8.57^{+6.29}_{-2.90}$	$0.0032^{+0.0002}_{-0.0002}$	115.8	−	$18.41^{+11.37}_{-6.86}$	−	28.72	151.80
SPT-CL J0456−5116	13474	44.6	04 56 27.64*	−51 16 43.7*	$10.24^{+6.76}_{-3.06}$	$0.0054^{+0.0004}_{-0.0004}$	62.2	−	$12.32^{+6.53}_{-4.26}$	$4.69^{+2.63}_{-1.83}$	35.82	326.68
SPT-CL J0509−5342	9432	26.0	05 09 21.35	−53 42 12.74	$4.65^{+1.48}_{-0.83}$	$0.012^{+0.001}_{-0.001}$	40.3	$12.16^{+7.11}_{-14.24}$	$3.23^{+1.44}_{-1.00}$	$1.40^{+0.64}_{-0.45}$	14.50	13.13
SPT-CL J0517−5430	15099	17.4	05 16 34.23*	−54 31 37.76*	$5.44^{+5.63}_{-1.83}$	$0.0038^{+0.0006}_{-0.0005}$	58.5	$2.26^{+1.43}_{-2.41}$	$11.24^{+11.20}_{-5.86}$	−	34.74	98.83
SPT-CL J0528−5300	9341,10862 11747,1187 11996,12092 13126	14.1,11.2 16.6,28.1 9.7,19.3 17.3	05 28 04.98*	−52 59 45.86*	$8.60^{+5.50*}_{-3.60}$	$0.0030^{+0.0002}_{-0.0002}$	200.0	−	$16.56^{+6.10}_{-4.78}$	$4.54^{+1.93}_{-1.62}$	27.43	114.54
SPT-CL J0534−5005	11748,12001 12002	24.7,18.0 25.5	05 33 37.97*	−50 05 46.31*	$5.47^{+3.00*}_{-1.54}$	$0.0023^{+0.0002}_{-0.0002}$	131.4	−	$21.78^{+9.03}_{-8.67}$	−	29.95	63.94
SPT-CL J0542−4100*	914	45.0	05 42 49.5*	−41 00 01*	$10.24^{+10.12}_{-4.36}$	$0.0077^{+0.0004}_{-0.0007}$	47.4	−	$8.93^{+5.87}_{-3.90}$	−	34.05	288.60
SPT-CL J0547−5345	9332,9336 10851,1173	13.2,26.1 7.8,12.0	05 46 36.97	−53 45 37.26	$9.68^{+7.18}_{-3.28}$	$0.013^{+0.001}_{-0.001}$	48.0	−	$4.05^{+3.36}_{-1.71}$	$2.59^{+2.36}_{-1.46}$	15.24	63.97
SPT-CL J0552−5709	11743,11871	16.1,18.6	05 51 34.61*	−57 08 44.9*	$4.33^{+5.93}_{-1.35}$	$0.0038^{+0.0009}_{-0.0009}$	54.7	$3.20^{+1.48}_{-1.18}$	$8.24^{+16.78}_{-5.79}$	$3.15^{+6.71}_{-3.00}$	27.24	48.14
SPT-CL J0555−6405	13404	9.6	05 55 29.57*	−64 06 03.94*	$4.69^{+5.74}_{-2.02}$	$0.0045^{+0.0007}_{-0.0006}$	61.4	$2.48^{+2.02}_{-3.12}$	$10.42^{+7.72}_{-5.98}$	$4.47^{+4.16}_{-3.60}$	30.70	48.81
ACT-CL J0559−5249	12264,13116 13117	37.7,21.3 39.6	05 59 42.95	−52 49 47.91	$8.96^{+5.66}_{-2.78}$	$0.0057^{+0.0004}_{-0.0004}$	53.0	−	$10.92^{+5.58}_{-3.52}$	$5.00^{+5.58}_{-2.20}$	37.23	272.52
ACT-CL J0616−5227	12261,13127	25.1, 8.641	06 16 34.37*	−52 27 09.61*	$3.63^{+2.63}_{-1.29}$	$0.016^{+0.008}_{-0.008}$	36.6	−	$2.02^{+4.86}_{-1.21}$	$1.23^{+2.97}_{-7.76}$	9.84	3.99
SPT-CL J0655−5234	13486	18.7	06 55 53.9*	−52 34 18.5*	$6.61^{+2.47}_{-1.47}$	$0.0026^{+0.0001}_{-0.0002}$	124.8	−	$21.75^{+5.92}_{-5.81}$	−	31.48	100.20

Table 1 *– continued*

System[a]	Obs. ID[b]	t^c (ks)	X-ray core (J2000)[d] RA	Dec.	kT^e (keV)	n_e^f (cm^{-3})	r^g (kpc)	$\Delta(kT)^h$	t_{cool}^i (Gyr)	t_{cool} (10 kpc)^j (Gyr)	$\frac{t_{cool}}{t_{ff}}^k$	η_{min}^l
ACT-CL J0707−5522	12271	18.3	07 07 04.73*	−55 23 21.14*	$10.04^{+6.26}_{-3.31}$	$0.004^{+0.000}_{-0.000}$	77.1	–	$16.82^{+5.67}_{-5.54}$	$4.25^{+1.63}_{-1.61}$	31.02	227.45
SPT-CL J2011−5725*	4995	20.7	20 11 26.8	−57 25 12.68	$3.14^{+1.19}_{-0.82}$	$0.027^{+0.005}_{-0.005}$	16.6	$1.63^{+0.48}_{-0.64}$	$1.20^{+0.85}_{-0.74}$	$1.04^{+0.74}_{-0.65}$	11.35	4.88
SPT-CL J2023−5535	15108	16.2	20 23 21.84*	−55 35 47.78*	$11.73^{+12.24}_{-4.70}$	$0.0041^{+0.0002}_{-0.0003}$	64.6	–	$18.44^{+11.37}_{-7.69}$	–	51.60	830.07
SPT-CL J2031−4037	13517	8.7	20 31 52.6*	−40 37 27.45*	$8.00^{+3.45}_{-1.99}$	$0.0082^{+0.0004}_{-0.0004}$	67.0	$1.86^{+0.81}_{-0.70}$	$6.72^{+2.68}_{-1.80}$	–	18.12	54.80
SPT-CL J2034−5936	12182	54.6	20 34 09.11*	−59 36 16.58*	$10.54^{+33.67}_{-5.31}$	$0.006^{+0.001}_{-0.002}$	48.2	–	$8.93^{+27.72}_{-7.58}$	–	33.50	371.32
SPT-CL J2035−5251	13466	16.3	20 35 11.19*	−52 51 22.23*	$4.28^{+5.53}_{-0.88}$	$0.0018^{+0.0009}_{-0.0003}$	87.1	$2.52^{+1.88}_{-1.34}$	$14.12^{+30.70}_{-10.86}$	$5.05^{+11.26}_{-4.60}$	29.30	63.92
SPT-CL J2043−5035	13478	71.6	20 43 17.74	−50 35 32.32	$4.13^{+2.05}_{-1.20}$	$0.09^{+0.01}_{-0.01}$	8.9	$2.09^{+0.50}_{-0.43}$	$0.496^{+0.191}_{-0.205}$	$0.501^{+0.192}_{-0.206}$	10.06	0.482
SPT-CL J2106−5845	12189	43.4	21 06 05.3	−58 44 31.2	$3.95^{+1.37}_{-0.93}$	$0.015^{+0.000}_{-0.000}$	60.6	$3.31^{+2.56}_{-1.54}$	$2.804^{+0.574}_{-0.789}$	$0.923^{+0.204}_{-0.271}$	8.36	2.80
ACT-CL J2129−0005*	9370	28.8	21 29 39.9	00 05 21.6	$2.91^{+0.42}_{-0.30}$	$0.076^{+0.013}_{-0.012}$	6.4	$4.82^{+2.58}_{-1.50}$	$0.25^{+0.18}_{-0.12}$	–	6.93	2.03
SPT-CL J2135−5726	13463	14.9	21 35 38.373	−57 26 27.55	$7.73^{+3.43}_{-2.12}$	$0.0055^{+0.0003}_{-0.0003}$	74.2	–	$11.06^{+3.03}_{-2.82}$	$4.92^{+2.22}_{-2.16}$	26.94	99.93
SPT-CL J2145−5644	13398	12.0	21 45 52.418	−56 44 48.95	$17.93^{+17.13}_{-6.59}$	$0.0055^{+0.0005}_{-0.0006}$	82.2	–	$12.33^{+11.75}_{-6.62}$	$5.28^{+5.28}_{-3.26}$	27.08	460.98
SPT-CL J2146−4632	13469	71.7	21 46 34.67*	−46 32 58.5*	$10.55^{+10.20}_{-3.75}$	$0.0027^{+0.0003}_{-0.0003}$	104.5	–	$23.30^{+20.63}_{-11.55}$	$11.06^{+11.91}_{-8.72}$	40.27	460.98
SPT-CL J2148−6116	13488	29.1	21 48 44.43*	−61 16 41.63*	$6.40^{+2.43}_{-1.72}$	$0.0035^{+0.0000}_{-0.0000}$	102.8	$3.12^{+2.94}_{-2.11}$	$15.53^{+3.00}_{-3.22}$	$4.63^{+1.92}_{-1.97}$	27.30	74.50
ACT-CL J2154−0049	16230	55.7	21 54 32.2	−00 48 59.6	$8.24^{+5.59}_{-2.56}$	$0.0137^{+0.0008}_{-0.0007}$	29.6	–	$4.30^{+2.22}_{-0.96}$	$4.22^{+2.47}_{-1.50}$	26.22	125.24
SPT-CL J2218−4519	13501	31.2	22 18 59.06*	−45 18 55.4*	$8.12^{+12.08}_{-2.41}$	$0.0030^{+0.0002}_{-0.0002}$	112.5	–	$17.85^{+19.85}_{-6.48}$	$5.48^{+6.44}_{-2.88}$	28.66	146.61
SPT-CL J2222−4834	13497	27.9	22 22 50.9	−48 34 36.14	$4.59^{+1.47}_{-1.12}$	$0.015^{+0.001}_{-0.001}$	40.1	$1.90^{+0.96}_{-0.86}$	$3.14^{+0.78}_{-0.94}$	$1.64^{+0.44}_{-0.52}$	14.46	10.57
SPT-CL J2232−6000	13502	29.8	22 32 33.7	−59 59 53.89	$4.87^{+0.99}_{-0.84}$	$0.0129^{+0.0009}_{-0.0005}$	44.2	$1.51^{+0.45}_{-0.49}$	$2.64^{+0.85}_{-0.83}$	$0.94^{+0.31}_{-0.31}$	10.78	9.35
SPT-CL J2233−5339	13504	15.8	22 33 16.8*	−53 39 07.4*	$5.52^{+2.35}_{-1.30}$	$0.0063^{+0.0004}_{-0.0004}$	74.9	$1.57^{+1.13}_{-0.87}$	$6.78^{+3.28}_{-2.22}$	–	16.36	23.22
SPT-CL J2236−4555	13507,15266	41.3,32.4	22 36 52.18*	−45 55 51.7*	$11.15^{+5.36*}_{-3.46}$	$0.0084^{+0.0004}_{-0.0005}$	71.0	–	$8.65^{+3.14}_{-2.70}$	–	22.02	140.72
SPT-CL J2245−6207	13499	26.2	22 45 01.8*	−62 07 44.85*	$8.26^{+5.51}_{-2.67}$	$0.0026^{+0.0002}_{-0.0003}$	119.7	$3.82^{+6.02}_{-3.18}$	$19.73^{+14.93}_{-8.77}$	$4.40^{+4.40}_{-2.72}$	29.78	171.87
SPT-CL J2248−4431*	4966	21.2	22 48 44.5*	−44 31 48.5*	$15.39^{+11.20}_{-4.36}$	$0.027^{+0.002}_{-0.002}$	25.6	–	$2.65^{+1.70}_{-0.96}$	$2.24^{+1.49}_{-0.93}$	10.11	37.93
SPT-CL J2258−4044	13495	48.2	22 58 49.89*	−40 44 20.07*	$5.81^{+2.31}_{-1.45}$	$0.0054^{+0.0004}_{-0.0003}$	86.0	$4.23^{+2.25}_{-1.73}$	$9.32^{+3.21}_{-2.80}$	–	19.57	32.09
SPT-CL J2259−6057	13498	57.3	22 59 01.04	−60 57 38.44	$9.34^{+3.87}_{-2.57}$	$0.0139^{+0.0005}_{-0.0006}$	39.7	–	$4.85^{+135}_{-1.22}$	$3.20^{+1.10}_{-1.02}$	22.09	98.70
SPT-CL J2301−4023	13505	53.4	23 01 53.13	−40 23 06.51	$9.68^{+5.91}_{-2.78}$	$0.0093^{+0.0004}_{-0.0004}$	55.4	–	$7.32^{+2.22}_{-2.02}$	$2.77^{+0.90}_{-0.83}$	23.89	125.02
SPT-CL J2306−6505	13503	21.5	23 06 55.9*	−65 05 15.8*	$4.33^{+2.19}_{-1.03}$	$0.0020^{+0.0004}_{-0.0003}$	126.9	–	$17.73^{+13.83}_{-8.42}$	–	25.24	35.71
SPT-CL J2325−4111*	13405	7.4	23 25 11.47*	−41 12 13.3*	$5.57^{+10.40*}_{-2.40}$	$0.0045^{+0.0006}_{-0.0009}$	61.6	$2.73^{+2.20}_{-5.16}$	$10.68^{+14.21}_{-6.73}$	–	31.30	75.55
SPT-CL J2331−5051	9333	26.9	23 31 51.307	−50 51 53.77	$5.57^{+2.79}_{-1.59}$	$0.032^{+0.003}_{-0.002}$	24.2	$2.59^{+2.44}_{-1.24}$	$1.49^{+0.67}_{-0.57}$	$0.828^{+0.372}_{-0.319}$	11.13	10.04
SPT-CL J2335−4544	13496	18.0	23 35 08.42	−45 44 23.67	$10.63^{+4.12}_{-3.13}$	$0.0048^{+0.0002}_{-0.0002}$	99.1	–	$15.01^{+3.93}_{-3.71}$	$5.07^{+1.96}_{-1.91}$	27.37	191.87
ACT-CL J2337−0016*	11728	15.7	23 37 58.0	00 16 11.17	$9.4^{+14.6}_{-2.9}$	$0.0051^{+0.0005}_{-0.0006}$	58	–	$11.54^{+13.37}_{-5.10}$	–	36.13	305.57
SPT-CL J2337−5942	11859	17.5	23 37 25.09*	−59 42 20.59*	$5.64^{+5.27}_{-1.82}$	$0.0064^{+0.0008}_{-0.0006}$	87.7	$3.09^{+3.45}_{-3.18}$	$6.88^{+5.76}_{-3.23}$	$3.51^{+3.61}_{-2.66}$	14.18	17.76
SPT-CL J2341−5119	9345,11799	28.2,47.0	23 41 12.49	−51 19 44.17	$4.47^{+0.91}_{-1.19}$	$0.029^{+0.003}_{-0.002}$	25.6	$3.41^{+2.16}_{-1.39}$	$1.60^{+0.30}_{-0.45}$	$1.39^{+0.35}_{-0.45}$	11.29	6.19
SPT-CL J2343−5411	11741,11870 12014,12091	58.1,16.7 53.0,35.4	23 42 46.27	−54 11 05.83	$3.36^{+1.64}_{-0.81}$	$0.020^{+0.003}_{-0.005}$	28.0	$2.05^{+4.24}_{-1.12}$	$1.49^{+1.82}_{-1.04}$	$0.762^{+0.930}_{-0.532}$	9.63	3.479

Table 1 – *continued*

System[a]	Obs. ID[b]	t[c] (ks)	X-ray core (J2000)[d] RA	Dec.	kT[e] (keV)	n_e[f] (cm^{-3})	r[g] (kpc)	$\Delta(kT)$[h]	t_{cool}[i] (Gyr)	t_{cool} (10 kpc)[j] (Gyr)	$\frac{t_{cool}}{t_{ff}}$[k]	η_{min}[l]
SPT-CL J2344−4242*	13401	11.1	23 44 43.96	−42 43 12.7	$12.65^{+1.48}_{-1.70}$	$0.087^{+0.001}_{-0.001}$	41.0	$1.03^{+0.22}_{-0.19}$	$0.7991^{+0.0983}_{-0.1080}$	$0.438^{+0.0550}_{-0.0603}$	3.53	5.33
SPT-CL J2345−6406	13500	55.1	23 45 00.16*	−64 05 49.0*	$4.09^{+1.33}_{-0.98}$	$0.005^{+0.0005}_{-0.0004}$	95.0	$5.58^{+2.50}_{-4.49}$	$8.25^{+3.88}_{-1.75}$	$2.67^{+1.45}_{-0.92}$	15.68	9.81
SPT-CL J2352−4657	13506	68.7	23 52 16.25*	−46 57 35.97*	$3.57^{+0.77}_{-0.68}$	$0.0047^{+0.0004}_{-0.0003}$	81.0	$2.55^{+3.70}_{-1.30}$	$8.61^{+3.53}_{-1.45}$	$5.02^{+2.88}_{-2.19}$	19.34	11.45
SPT-CL J2355−5056	11746,11998	11.2,9.6	23 55 47.39	−50 55 40.58	$3.26^{+0.58}_{-0.41}$	$0.007^{+0.002}_{-0.003}$	34.3	$1.53^{+0.42}_{-0.34}$	$2.09^{+4.25}_{-1.75}$	$1.04^{+2.14}_{-0.94}$	11.02	8.27
SPT-CL J2359−5009	9334,11742 1864,11997	24.3,21.0 18.5,58.6	23 59 43.56*	−50 10 15.87*	$5.13^{+5.88}_{-1.64}$	$0.004^{+0.001}_{-0.001}$	54.8	–	$7.06^{+16.95}_{-5.66}$	–	23.29	57.64

[a]Alternative names for ACT-CL J0102−4915 (El Gordo); ACT-CL J0152−0100 (A267); ACT-CL J0245−5302 (AS0295); ACT-CL J0326−0043 iiiC(MACS J0326−0043); SPT-CL J0542−4100 (RDCS J0542−4100); SPT-CL J2011.3−5725 (RXCJ2011.3−5725); ACT-CL J2129−0005 (RXJ2129.6+0005); SPT-CL J2248−4431 (AS1063); SPT-CL J2325−4111 (ACOS1121); ACT-CL J2337−0016 (A2631); SPT-CL J2344−4242 (Phoenix cluster).

[b]Some systems have multiple *Chandra* observations: e.g. SPT-CL J0151−5954 (Obs. IDs 13480 and 14380).

[c]The time on source after reprocessing the data.

[d]The X-ray core position from this work; the asterisks mark the systems with uncertain core positions.

[e]Central-bin temperature (innermost region used for deprojection). The systems marked with asterisk are the ones with only two bins for deprojection (see the text).

[f]Central-bin electron density (innermost region used for deprojection).

[g]The radius for the innermost region used for spectral deprojection.

[h]The temperature drop is calculated as the ratio between the highest and the lowest temperatures of the profile when the profile is rising upward smoothly. For the systems which do not have a statistically significant temperature drop or their temperature profile is rising inwardly there is no entry for the temperature drop.

[i]The cooling time of the innermost region (in Gyr).

[j]The cooling time at 10 kpc derived using the deprojected SB profiles (in Gyr). In some cases, the SB deprojection did not work well (due, e.g. to the SB profile dropping or flattening towards the centre). In these cases, there is no entry for the cooling time at 10 kpc.

[k]The ratio of the cooling time to free-fall time.

[l]Thermal-stability parameter from Voit et al. (2008); Inst. $= \min(kT/\Lambda n_e n_H r^2)$. For some of the systems, the instability profile is still rising, therefore there is no minimum (e.g. A399, A3158, A754, and A2163). See the text for details.

Table 2. Cluster and cRS properties.

System[a]	z	$L_X(<r_{cool})$ $(10^{42}$ erg s$^{-1})$	r_{cool} (kpc)	M_{500}^{SZ} $(10^{14}$ M$_\odot)$	$L_X(<R_{500})$ $(10^{42}$ erg s$^{-1})$	R_{500} (kpc)	$L_{843MHz}[b]$ $(10^{32}$ erg s^{-1} Hz$^{-1})$	SFR[c] $(M_\odot$ yr$^1)$
				CF Sample				
SPT-CL J0000−5748	0.7019(1)	868^{+67}_{-48}	130	4.29 ± 0.71 (5)	1078^{+61}_{-71}	679	8.83 ± 0.33	52^{+59}_{-30}
SPT-CL J0033−6326	0.597 (5)	178^{+17}_{-18}	101	4.72 ± 0.88 (1)	627^{+59}_{-65}	766	<0.88	<43
ACT-CL J0102−4915*	0.87 (5)	589^{+10}_{-9}	152	14.43 ± 2.1 (1)	10867^{+188}_{-156}	894	0.16 ± 0.03	93^{+120}_{-55}
SPT-CL J0232−4420*	0.284 (5)	930^{+33}_{-29}	125	12.01 ± 1.80 (1)	2105^{+76}_{-69}	1333	1.27 ± 0.08	17^{+19}_{-10}
SPT-CL J0234−5831	0.415(1)	836^{+86}_{-67}	130	7.64 ± 1.5 (5)	1246^{+86}_{-81}	1040	2.60 ± 0.10	59^{+35}_{-22}
ACT-CL J0304−4921	0.392 (5)	464^{+29}_{-24}	100	7.57 ± 1.2 (1)	1136^{+57}_{-55}	1053	$0.11 \pm 0.01*$	<15
ACT-CL J0326−0043*	0.448 (4)	1709^{+90}_{-75}	660	7.4 ± 1.4 (2)	1709^{+77}_{-95}	1000	0.17 ± 0.02	–
SPT-CL J0334−4659	0.485 (5)	429^{+16}_{-16}	125	5.52 ± 0.95 (1)	836^{+43}_{-54}	881	1.10 ± 0.08	79^{+45}_{-39}
SPT-CL J0417−4748	0.581 (5)	1268^{+50}_{-62}	142	7.41 ± 1.15 (1)	2209^{+137}_{-92}	901	<1.38	<28
ACT-CL J0616−5227	0.684 (6)	258^{+9}_{-22}	107	6.8 ± 2.9 (3)	1021^{+76}_{-77}	807	6.99 ± 0.31	–
SPT-CL J2011−5725*	0.2786 (1)	301^{+12}_{-10}	131	3.18 ± 0.89 (5)	373^{+15}_{-14}	869	<0.15	–
SPT-CL J2043−5035	0.7234 (1)	1375^{+35}_{-38}	287	4.71 ± 1.0 (5)	1653^{+59}_{-50}	696	<1.41	160^{+123}_{-69}
SPT-CL J2106−5845	1.132 (1)	1201^{+55}_{-60}	146	8.36 ± 1.71 (5)	3218^{+219}_{-193}	610	8.73 ± 0.99	200^{+240}_{-100}
ACT-CL J2129−0005*	0.234 (4)	638^{+15}_{-15}	101	7.3 ± 1.6 (2)	1186^{+33}_{-32}	1171	0.690 ± 0.03	–
SPT-CL J2232−6000	0.594 (5)	312^{+19}_{-15}	110	5.55 ± 0.97 (1)	726^{+48}_{-49}	810	<0.87	<33
SPT-CL J2331−5051	0.576 (1)	662^{+42}_{-36}	116	5.14 ± 0.71 (5)	929^{+75}_{-66}	801	1.80 ± 0.134	23^{+36}_{-14}
SPT-CL J2341−5119	1.003 (1)	364^{+30}_{-22}	77	5.61 ± 0.82 (5)	1604^{+88}_{-107}	588	4.15 ± 0.58	<170
SPT-CL J2343−5411	1.075 (1)	318^{+44}_{-48}	116	3.0 ± 0.5 (5)	542^{+53}_{-19}	452	<3.75	33^{+42}_{-19}
SPT-CL J2344−4242*	0.595 (2)	13913^{+273}_{-318}	173	12.5 ± 1.57 (6)	13913^{+335}_{-270}	1061	11.57 ± 0.41	1900^{+926}_{-525}
SPT-CL J2355−5056	0.3196 (1)	85^{+6}_{-8}	93	4.07 ± 0.57 (5)	312^{+21}_{-23}?	908	<0.20	–
				NCF sample				
SPT-CL J0013−4906	0.406 (5)	205^{+19}_{-15}	67	7.08 ± 1.15(1)	1214^{+81}_{-86}	1019	<0.60	<8.6
ACT-CL J0014−0056	0.533 (4)	270^{+16}_{-24}	80	7.6 ± 1.4 (2)	1281^{+58}_{-62}	944	<0.47	–
SPT-CL J0014−4952	0.752 (2)	123^{+95}_{-48}	78	5.31 ± 0.92 (1)	1292^{+70}_{-72}	704	<2.59	<92
ACT-CL J0022−0036	0.805 (4)	76^{+9}_{-10}	47	7.3 ± 1.2 (2)	1688^{+134}_{-112}	750	9.55 ± 0.36	–
SPT-CL J0040−4407	0.35 (2)	349^{+26}_{-26}	61	10.18 ± 1.32 (6)	1285^{+68}_{-62}	1200	<0.41	<14
SPT-CL J0058−6145	0.83 (5)	84^{+8}_{-15}	57	4.36 ± 0.81 (1)	514^{+48}_{-39}	619	2.60 ± 0.33	24^{+34}_{-13}
ACT-CL J0059−0049	0.786 (4)	142^{+13}_{-17}	69	6.9 ± 1.2 (2)	1421^{+90}_{-90}	747	<1.20	–
SPT-CL J0102−4603	0.72 (5)	21^{+5}_{-3}	66	4.49 ± 0.85 (1)	229^{+36}_{-32}	683	<2.33	15^{+20}_{-9}
SPT-CL J0106−5943	0.348 (5)	86^{+8}_{-8}	58	6.23 ± 1.05 (1)	516^{+32}_{-29}	1620	0.23 ± 0.08	<7.3
SPT-CL J0123−4821	0.62 (5)	12^{+4}_{-2}	32	4.46 ± 0.87 (1)	337^{+27}_{-24}	738	$<0.113*$	<39
SPT-CL J0142−5032	0.73 (5)	49^{+39}_{-19}	40	5.75 ± 0.95 (1)	760^{+84}_{-80}	735	$<0.19*$	92^{+54}_{-34}
SPT-CL J0151−5954	0.29 (5)	$0.80^{+0.89}_{-0.52}$	17	3.24 ± 0.90 (1)	22^{+5}_{-4}	857	0.37 ± 0.04	<140
ACT-CL J0152−0100*	0.23 (4)	133^{+5}_{-4}	67	7.9 ± 1.6 (2)	978^{+35}_{-29}	1206	0.068 ± 0.009	–
SPT-CL J0156−5541	1.22 (5)	242^{+27}_{-18}	58	3.63 ± 0.70 (1)	874^{+72}_{-72}	432	<5.12	<530
SPT-CL J0200−4852	0.498 (5)	106^{+29}_{-42}	49	4.76 ± 0.90 (1)	498^{+32}_{-39}	830	<0.95	<29
ACT-CL J0206−0114	0.676 (4)	340^{+18}_{-26}	76	5.7 ± 1.1 (2)	860^{+47}_{-39}	766	3.18 ± 0.17	–
SPT-CL J0212−4657	0.655 (5)	50^{+6}_{-6}	66	5.88 ± 0.98 (1)	327^{+20}_{-24}	787	$<0.77*$	<49
ACT-CL J0215−5212	0.48 (6)	96^{+17}_{-27}	69	5.8 ± 1.7 (3)	378^{+49}_{-39}	900	4.33 ± 0.17	–
ACT-CL J0217−5245	0.34 (3)	–	–	4.42 ± 0.89 (1)	305^{+47}_{-34}	916	0.91 ± 0.05	<9.2
ACT-CL J0232−5257	0.556 (5)	–	–	5.36 ± 0.94 (1)	815^{+74}_{-88}	825	<0.74	<26
ACT-CL J0235−5121	0.278 (5)	–	–	6.41 ± 1.08 (1)	564^{+30}_{-30}	1086	0.16 ± 0.03	<14
ACT-CL J0237−4939	0.334 (5)	–	–	3.99 ± 0.86 (1)	241^{+21}_{-18}	889	<0.370	–
SPT-CL J0243−5930	0.65(1)	232^{+17}_{-17}	90	4.18 ± 0.89 (5)	969^{+77}_{-70}	709	<1.09	<35
ACT-CL J0245−5302*	0.3 (3)	69^{+6}_{-7}	46	6.6 ± 1.0 (4)	1807^{+57}_{-63}	1079	0.317 ± 0.043	–
SPT-CL J0252−4824	0.421 (5)	8^{+2}_{-2}	34	4.79 ± 0.93 (1)	350^{+24}_{-29}	884	<0.64	<5.9
SPT-CL J0256−5617	0.64(1)	–	–	4.25 ± 0.89 (5)	852^{+80}_{-77}	718	<1.05	<35
SPT-CL J0304−4401	0.458 (5)	64^{+10}_{-7}	53	8.55 ± 1.32 (1)	949^{+56}_{-61}	1042	$<0.028*$	<6.1
SPT-CL J0307−5042	0.55 (5)	77^{+8}_{-4}	74	5.26 ± 0.93 (1)	622^{+41}_{-40}	824	$<0.334*$	<25

Table 2 – *continued*

System[a]	z	$L_X(<r_{cool})$ (10^{42} erg s^{-1})	r_{cool} (kpc)	M_{500}^{SZ} (10^{14} M$_\odot$)	$L_X(<R_{500})$ (10^{42} erg s^{-1})	R_{500} (kpc)	$L_{843MHz}{}^b$ (10^{32} erg s^{-1} Hz^{-1})	SFR[c] (M$_\odot$ yr^1)
SPT-CL J0307−6225	0.59(1)	73^{+16}_{-17}	97	4.68 ± 0.96 (5)	497^{+49}_{-51}	772	2.69 ± 0.19	<44
SPT-CL J0310−4646	0.709 (5)	117^{+11}_{-18}	69	4.31 ± 0.83 (1)	606^{+86}_{-67}	679	<2.24	34^{+21}_{-13}
SPT-CL J0324−6236	0.72(1)	–	–	4.68 ± 0.86 (5)	642^{+320}_{-136}	696	3.98 ± 0.25	<57
ACT-CL J0346−5438	0.53 (5)	58^{+11}_{-11}	49	5.47 ± 0.94 (1)	625^{+56}_{-69}	848	2.93 ± 0.12	<5.7
SPT-CL J0348−4514	0.358 (5)	64^{+8}_{-6}	80	6.17 ± 1.03 (1)	557^{+49}_{-45}	1010	$<0.0668*$	<5.7
SPT-CL J0352−5647	0.66(1)	80^{+11}_{-9}	74	4.00 ± 0.86 (5)	448^{+31}_{-34}	693	<1.13	<50
SPT-CL J0406−4804	0.737 (5)	82^{+25}_{-25}	61	4.61 ± 0.83 (1)	520^{+61}_{-48}	679	<2.46	41^{+26}_{-15}
SPT-CL J0411−4819	0.424 (5)	202^{+8}_{-9}	74	8.18 ± 1.27 (1)	1286^{+62}_{-52}	1054	$<0.639*$	27^{+5}_{-11}
SPT-CL J0426−5455	0.62(1)	–	–	4.93 ± 1.00 (5)	517^{+48}_{-51}	766	<0.97	51^{+41}_{-22}
ACT-CL J0438−5419	0.421 (5)	909^{+33}_{-33}	119	10.8 ± 1.62 (1)	3460^{+132}_{-116}	1159	<0.38	<24
SPT-CL J0441−4854	0.79 (5)	265^{+21}_{-24}	89	4.74 ± 0.83 (1)	789^{+83}_{-71}	657	<2.92	<61
SPT-CL J0446−5849	1.16 (5)	–	–	3.68 ± 0.82 (5)	711^{+178}_{-107}	440	<4.82	330^{+270}_{-170}
SPT-CL J0449−4901	0.79 (2)	–	–	4.57 ± 0.86 (6)	653^{+60}_{-68}	649	18.66 ± 0.96	88^{+110}_{-47}
SPT-CL J0456−5116	0.562 (5)	38^{+6}_{-7}	47	5.09 ± 0.89 (1)	483^{+36}_{-33}	807	4.34 ± 0.19	<32
SPT-CL J0509−5342	0.4626(1)	207^{+13}_{-11}	90	5.36 ± 0.71 (5)	769^{+50}_{-38}	309	<0.48	33^{+30}_{-12}
SPT-CL J0517−5430	0.295(1)	13^{+12}_{-5}	36	6.46 ± 1.32 (5)	1090^{+47}_{-52}	1081	<0.17	$2.5^{+1.3}_{-0.82}$
SPT-CL J0528−5300	0.7648(1)	–	–	3.18 ± 0.61 (5)	182^{+36}_{-37}	589	16.50 ± 0.54	<34
SPT-CL J0534−5005	0.881(1)	–	–	2.68 ± 0.61 (5)	417^{+127}_{-95}	510	<2.29	50^{+29}_{-19}
SPT-CL J0542−4100*	0.642 (5)	78^{+24}_{-25}	41	5.16 ± 0.94 (1)	612^{+41}_{-43}	761	8.53 ± 0.33	<28
SPT-CL J0547−5345	1.067 (1)	453^{+52}_{-58}	90	5.25 ± 0.75 (5)	1599^{+106}_{-141}	549	<3.68	110^{+89}_{-53}
SPT-CL J0552−5709	0.423 (1)	212^{+11}_{-13}	51	3.75 ± 0.54 (5)	450^{+34}_{-35}	818.329	1.46 ± 0.10	<17
SPT-CL J0555−6405	0.345 (5)	21^{+8}_{-5}	39	7.69 ± 1.22 (1)	436^{+20}_{-22}	1097	<0.24	–
ACT-CL J0559−5249	0.609 (5)	32^{+15}_{-14}	31	5.78 ± 0.95 (1)	556^{+34}_{-35}	811	7.88 ± 0.42	<19
SPT-CL J0655−5234	0.47 (5)	–	–	5.1 ± 0.93 (1)	296^{+29}_{-31}	869	<0.50	<3.1
ACT-CL J0707−5522	0.296 (7)	–	–	5.7 ± 1.7 (7)	580^{+30}_{-26}	1030	0.17 ± 0.02	–
SPT-CL J2023−5535	0.232 (1)	39^{+20}_{-17}	29	7.86 ± 1.24 (1)	952^{+31}_{-27}	1202	0.26 ± 0.02	–
SPT-CL J2031−4037	0.342 (5)	289^{+25}_{-24}	78	9.83 ± 1.5 (1)	1550^{+62}_{-73}	1193	1.645 ± 0.070	<7.5
SPT-CL J2034−5936	0.92 (1)	132^{+16}_{-17}	71	4.32 ± 0.89 (5)	741^{+36}_{-54}	577	3.91 ± 0.60	<99
SPT-CL J2035−5251	0.47 (1)	271^{+23}_{-22}	47	6.18 ± 1.25 (5)	402^{+77}_{-51}	930	1.14 ± 0.91	31^{+29}_{-16}
SPT-CL J2135−5726	0.427 (1)	–	–	5.68 ± 1.11 (5)	705^{+50}_{-46}	935	0.35 ± 0.09	<13
SPT-CL J2145−5644	0.48 (1)	112^{+13}_{-17}	48	6.39 ± 1.25 (5)	1181^{+106}_{-105}	933	<0.52	<3.6
SPT-CL J2146−4632	0.933 (1)	–	–	5.36 ± 1.07 (5)	814^{+69}_{-59}	614	15.49 ± 0.62	<9.6
SPT-CL J2148−6116	0.571 (1)	–	–	4.04 ± 0.89 (5)	546^{+35}_{-34}	746	1.69 ± 0.21	<39
ACT-CL J2154−0049	0.488 (4)	100^{+6}_{-9}	61	5.7 ± 1.3 (2)	485^{+25}_{-28}	889	<0.38	–
SPT-CL J2218−4519	0.65 (5)	–	–	5.31 ± 0.92 (1)	558^{+55}_{-59}	763	9.18 ± 0.67	$4.4^{+5}_{-2.4}$
SPT-CL J2222−4834	0.652 (5)	175^{+10}_{-15}	84	5.42 ± 0.93 (1)	670^{+70}_{-59}	767	<1.82	<52
SPT-CL J2233−5339	0.48 (5)	312^{+20}_{-17}	85	5.48 ± 0.98 (1)	819^{+55}_{-49}	883	<0.52	<13
SPT-CL J2236−4555	1.16 (5)	–	–	4.02 ± 0.74 (1)	776^{+70}_{-64}	467	<7.54	50^{+60}_{-30}
SPT-CL J2245−6206	0.58 (5)	46^{+21}_{-14}	55	5.4 ± 0.94 (1)	1250^{+86}_{-118}	812	12.59 ± 0.40	<5.2
SPT-CL J2248−4431*	0.351 (2)	2370^{+43}_{-52}	142	17.97 ± 2.18 (6)	6951^{+128}_{-114}	1449	0.64 ± 0.21	–
SPT-CL J2258−4044	0.83 (5)	85^{+15}_{-12}	73	5.88 ± 0.95 (1)	941^{+83}_{-78}	684	$<5.82*$	$10^{+12}_{-5.7}$
SPT-CL J2259−6057	0.75 (5)	235^{+18}_{-17}	74	5.61 ± 0.94 (1)	1032^{+80}_{-74}	718	13.90 ± 0.44	<84
SPT-CL J2301−4023	0.73 (5)	114^{+8}_{-7}	59	4.81 ± 0.86 (1)	625^{+3}_{-12}	693	$0.86 \pm 0.02*$	36^{+53}_{-19}
SPT-CL J2306−6505	0.53 (5)	20^{+16}_{-8}	36	5.73 ± 0.98 (1)	642^{+64}_{-52}	861	<0.66	<39
SPT-CL J2325−4111*	0.358 (5)	25^{+7}_{-5}	40	7.55 ± 1.2 (1)	756^{+43}_{-39}	1080	<0.43	<6.7
SPT-CL J2335−4544	0.547 (5)	–	–	6.17 ± 1.02 (1)	870^{+65}_{-67}	871	1.56 ± 0.14	41^{+61}_{-27}
ACT-CL J2337−0016*	0.275 (4)	38^{+6}_{-4}	43	8.4 ± 1.7 (2)	1031^{+48}_{-38}	1191	<0.098	—
SPT-CL J2337−5942	0.775 (1)	387^{+35}_{-34}	98	8.14 ± 1.14 (5)	2108^{+128}_{130}	799	<1.67	$1.0^{+1.5}_{-0.7}$
SPT-CL J2345−6406	0.94 (5)	106^{+8}_{-15}	89	5.1 ± 0.86 (1)	792^{+72}_{-51}	599	<2.59	250^{+130}_{-89}

Table 2 – *continued*

System[a]	z	$L_X(<r_{cool})$ (10^{42} erg s^{-1})	r_{cool} (kpc)	M_{500}^{SZ} (10^{14} M$_\odot$)	$L_X(<R_{500})$ (10^{42} erg s^{-1})	R_{500} (kpc)	L_{843MHz}[b] (10^{32} erg s^{-1}Hz^{-1})	SFR[c] (M$_\odot$ yr^1)
SPT-CL J2352−4657	0.73 (5)	–	–	4.42 ± 0.83 (1)	141_{-24}^{+40}	674	<2.40	<9.5
SPT-CL J2359−5009	0.775 (1)	35_{-8}^{+14}	62	3.54 ± 0.54 (5)	281_{-30}^{+41}	605	5.96 ± 0.31	$8.4_{-6.0}^{+13}$

References: (1) Bleem et al. (2015); (2) Hasselfield et al. (2013); (3) Hilton et al. (2013); (4) Marriage et al. (2011); (5) Reichardt et al. (2013); (6) Ruel et al. (2014); and (7) Sifón et al. (2013).

[a]Alternative names for ACT-CL J0102−4915 (El Gordo); ACT-CL J0152−0100 (A267); SPT-CL J0232−4420 (RXCJ0232.2−4420); ACT-CL J0245−5302 (AS0295); ACT-CL J0326−0043 (MACS J0326−0043); SPT-CL J0542−4100 (RDCS J0542−4100); SPT-CL J2011−5725 (RXCJ2011.3−5725); ACT-CL J2129−0005 (RXJ2129.6+0005); SPT-CL J2248−4431 (AS1063); SPT-CL J2325−4111 (ACOS1121); ACT-CL J2337−0016 (A2631); and SPT-CL J2344−4242 (Phoenix). The asterisk marks systems with uncertain core positions.

[b]Rest-frame monochromatic radio luminosity at 843 MHz using the flux densities from SUMSS (Bock et al. 1999), except ACT-CL J0014−0056, ACT-CL J0022−0036, ACT-CL J0059−0049, ACT-CL J0152−0100, ACT-CL J0206−0114, ACT-CL J2129−0005, ACT-CL J2154−0049, and ACT-CL J2337−0016 where NVSS flux densities were used (Condon et al. 1998); ACT-CL J0326−0043 where the FIRST flux density was used (Helfand et al. 2015); and for ACT-CL J0102−4915 and ACT-CL J0152−0100 where the GMRT flux density at 610 MHz from Lindner et al. (2014) and Kale et al. (2013), respectively, was used. The systems marked with asterisk are the ones for which we have GMRT data at 325 MHz (Intema et al. in preparation). For SPT-CL J0106−5943, SPT-CL J2135−5726, and SPT-CL J2248−4431, we measured the flux densities from SUMSS images (5.7 ± 1.9 mJy, 5.3 ± 2.5 mJy, and 15.4 ± 4.9 mJy, respectively). The numbers without errors are the upper limit using the noise in the SUMSS or NVSS image: 6–10 mJy beam^{-1} (depending on the declination) for SUMSS (Mauch et al. 2003) and 2.5 mJy beam^{-1} for NVSS (Condon et al. 1998).

[c]SFRs from McDonald et al. (2016).

Rafferty et al. 2008; Bîrzan et al. 2012), we define the cooling radius as the radius within which the gas has a cooling time less than 7.7×10^9 yr. To find the total luminosity inside the cooling radius, we performed the deprojection using a single-temperature model, extracting the spectra in annuli matched to this cooling radius (i.e. the outer radius of one annulus falls on the cooling radius). Table 1 gives the values of t_{cool} and Table 2 gives the values of r_{cool} and $L_X(<r_{cool})$. However, in some cases, it was not possible to measure a cooling region and an X-ray luminosity (e.g. for faint, diffuse clusters that are likely non-cooling flow(NCF) clusters).

Furthermore, we also fit the bolometric luminosity inside the R_{500} region, $L_X(<R_{500})$, and these values are listed in Table 2. R_{500} is defined as the region at which the mean mass density is 500 times the critical density at that cluster redshift (see Pratt et al. 2009). We calculated R_{500} using the masses, M_{500}, derived from the SZ signal Y_{SZ} (Reichardt et al. 2013; Hasselfield et al. 2013; Hilton et al. 2013; Bleem et al. 2015).[2]

3.2 Cooling flow clusters

We investigated three different diagnostics to identify the CF systems in our sample: central cooling time, the minimum thermal instability and the ratio of cooling time to free-fall time. Each of these diagnostics should be sensitive to the presence of gas that is unstable to cooling.

To calculate the central cooling times, we used the deprojection technique described in Section 3.1. The minimum radius at which we could derive reliable cooling times depends on the central SB (see Table 1 for the radius of the inner annulus used in the deprojection). Since we want to compare the cooling times for all the systems at a single physical radius, as close as possible to the nucleus, we computed the cooling time at 10 kpc using the SB profiles to extrapolate the densities inward (see Section 3.1). For some systems, the extrapolation did not work well, as the SB profile is too noisy or drops towards the centre or there is significant substructure that is inconsistent with the deprojection method (i.e. systems with large

SB errors, see Section 3.6). For these systems, we did not calculate a cooling time at 10 kpc, and these are the ones with missing values for $t_{cool}(10$ kpc) in Table 1.

Additionally, we calculated the central temperature drop for each system, since the temperature is expected to drop towards the centre in a CF cluster. We calculated the drop as the ratio between the highest temperature in the profile and the temperature of the innermost annulus. Table 1 lists the temperature drop values for all systems. Some systems have no entry since the temperature profile increases towards the centre, or the profile was too noisy and the temperature drop value was insignificant within errors. Generally, the calculated temperature drop depends on the size of the innermost annulus. However, the temperature typically varies slowly with radius, so variations in the size of the annuli should not affect our estimates significantly. We note that the temperature drop is not used in this paper as a criterion to separate the CF systems from NCF systems.

An alternative way to select CFs is based on the thermal stability of the gas (Voit et al. 2008, 2016; Sharma et al. 2012).Voit et al. (2008) found that SF and Hα emissions (and hence cooling) seem to occur only if, at some location in the cluster, the following condition is met:

$$\eta_{min} = \min\left(\frac{\kappa T}{\Lambda(T) n_e n_H r^2}\right) \sim \frac{1}{f_c} \lesssim 5, \tag{1}$$

where $\Lambda(T)$ is the cooling function calculated using the APEC spectral model (Smith et al. 2001), and f_c is the factor by which the magnetic field suppresses the conductivity below the *Spitzer* value. Assuming that the effective thermal conductivity can be expressed as a multiple, f_c, of the *Spitzer* value, this parameter provides a measure of the stability of the gas to local cooling. For large values of η_{min}, thermal conduction overwhelms radiative cooling, preventing local cooling throughout the ICM. For small values of this parameter, local cooling can run away, so that some regions of the ICM may cool to low temperatures, resulting in a multiphase medium and the deposition of the cooled gas.

If the AGN are fuelled by the cooled ICM, a process known in literature as the cold feedback mechanism (Pizzolato & Soker 2005, 2010), chaotic feedback (Gaspari, Ruszkowski & Oh 2013; Gaspari et al. 2015) or precipitation (Voit & Donahue 2015; Voit et al. 2015, 2016), then η_{min} determines the systems where cooling should

---

[2] $R_{500} = \left(\frac{M_{500}}{500\rho_c(z)4\pi/3}\right)^{1/3}$, with $\rho(z) = \frac{h(z)^2 3 H_0^2}{8\pi G}$ and $h(z)^2 = \Omega_M(1+z)^3 + \Omega_\Lambda$.

occur. Voit et al. (2008) found that values of $\eta_{min} \lesssim 5$ correspond approximately to an inner cooling time of 5×10^8 yr.

Recently, the multiphase threshold has been interpreted as resulting from the coupling between conduction and thermal instability (for a review, see Voit et al. 2016), since simulations have shown that thermal instability can produce a multiphase medium when the ratio of cooling time to free-fall time is $\lesssim 10$ (McCourt et al. 2012; Sharma et al. 2012; Gaspari et al. 2012). There are 22 systems in our sample which meet this multiphase threshold. Additionally, we find that a multiphase threshold of $t_{cool}/t_{ff} \lesssim 10$ corresponds to a central cooling time of $t_{cool}(10\,kpc) \lesssim 2 \times 10^9$ yr and $\eta_{min} \lesssim 10$, with two exceptions: SPT-CL J2248−4431 and ACT-CL J0438−5419, where $t_{cool}(10\,kpc) > 2 \times 10^9$ yr. These two systems show elongated X-ray morphologies, with higher central temperatures, and therefore may have gone through a merger recently. The 20 systems with $t_{cool}/t_{ff} \lesssim 10$, $t_{cool}(10\,kpc) \lesssim 2 \times 10^9$ yr and $\eta_{min} \lesssim 10$ are our sample of CF systems (see Section 4.3). Furthermore, there are eight intermediate systems with $t_{cool}(10\,kpc) \lesssim 2 \times 10^9$ yr, but $t_{cool}/t_{ff} > 10$, and four systems with $t_{cool}(10\,kpc) > 2 \times 10^9$ yr, $t_{cool}/t_{ff} > 10$, but $\eta_{min} \sim 10$.

Our sample of 20 CF systems is smaller than that of McDonald et al. (2013b), who identified 29 CF systems through their short central cooling times (a cooling time of the inner bin $\lesssim 10^9$ yr) from a similar parent sample. Our CF sample and the McDonald et al. (2013b) CF sample have 13 systems in common. Among the seven systems that are only in our CF sample, four systems were not analysed in the McDonald et al. (2013b) sample (e.g. some ACT systems); for the remaining three, McDonald et al. (2013b) did not find a short cooling time (e.g. El Gordo). For eight of the 16 CF systems that appear in the McDonald et al. (2013b) CF sample but not in ours, we obtain higher inner temperatures than those from the extrapolation used in McDonald et al. (2013b) The remaining eight systems are either borderline CFs or have large errors in their X-ray profiles.

3.3 Radio properties

The SPT and ACT southern sources are covered at 843 MHZ by the SUMSS (Bock, Large & Sadler 1999). The ACT galactic sources are covered by the NVSS at 1.4 GHz (Condon et al. 1998). For ACT-CL J0326−0043, we use the flux density at 1.4 GHz from the Faint Images of the Radio Sky at Twenty-cm (FIRST) survey (Helfand, White & Becker 2015), as the central source and an unrelated source at ∼80 kpc separation are blended together in the NVSS image (see Fig. 1). For ACT-CL J0102−4915 (El Gordo) and ACT-CL J0152−0100, we use the flux density from deep GMRT images at 610 MHz (Lindner et al. 2014; Kale et al. 2013). Additionally, for the following systems, we have obtained targeted GMRT observations at 325 MHz with integration times of 5.5 h per target (Intema et al. in preparation): SPT-CL J0123−4821, SPT-CL J0142−5032, SPT-CL J0212−4657, SPT-CL J0304−4401, ACT-CL J0304−4514, SPT-CL J0307−5042, SPT-CL J0348−4514, SPT-CL J0411−4819, SPT-CL J2031−4037, SPT-CL J2258−4044, and SPT-CL J2301−4023. These observations were made between 2014 May and November, and were reduced with the SPAM package (Intema et al. 2009; Intema 2014).

We searched the radio images for evidence of a central radio source (cRS). We consider a source to be a cRS if the peak of the emission lies within a radius of 2″ of the BCG optical core (when more than one BCG is present, we use the BCG that lies closest to the cluster X-ray core). The 2″ radius corresponds to the approximate positional accuracy of NVSS and SUMMS for sources with flux

densities typical of those in our sample ($\gtrsim 15$ mJy at the frequency of the survey Condon et al. 1998; Bock et al. 1999), and equates to uncertainties of ∼8–20 kpc for our sample, depending on the redshift of the source. Since this radius is typically within the envelope of the BCG and chance superposition of an unassociated source within this radius is unlikely (<0.001, Cavagnolo et al. 2008), we do not expect significant contamination by non-cRSs. In total, 46 sources in our sample have a detected cRS (two of which were found in our targeted GMRT observations: SPT-CL J2301−4023 and ACT-CL J0304−4921; see Figs 1 and 2).

Table 2 lists the rest-frame 843 MHz monochromatic radio luminosities for the cRSs, calculated as follows:

$$L_{843MHz} = 4\pi D_L^2 S_{843GHz}(1+z)^{\alpha-1}, \tag{2}$$

where α is the spectral index assuming $S_\nu \sim \nu^{-\alpha}$ and S_{843MHz} is the (observed-frame) flux density at 843 MHz. Since no spectral index information was available for the sources in our sample, a value of 1.0 was adopted.

For the systems with no detected cRS, Table 2 lists the upper limits from the SUMSS, NVSS, and GMRT images. The 5σ sensitivity limits of the SUMSS images are 6–10 mJy beam^{-1}, depending on the declination (Mauch et al. 2003). For the NVSS catalogue, the 5σ sensitivity limit is 2.5 mJy beam^{-1} at 1400 MHz (Condon et al. 1998), which implies a limit of 4.5 mJy beam^{-1} at our reference frequency of 843 MHz for a source with $\alpha = 1$. For our GMRT images at 325 MHz, we obtained 5σ sensitivities of 1–40 mJy beam^{-1} (Intema et al. in preparation), giving limits as low as 0.4 mJy beam^{-1} at 843 MHz.

We note that some sources may have a radio mini-halo in addition to the cRS (e.g. Mittal et al. 2009), and recently it was found that radio mini-haloes are common in massive CF clusters up to $z < 0.35$ (Giacintucci et al. 2017). For example, in SPT-CL J2344−4242 (the Phoenix cluster), van Weeren et al. (2014) found a probable radio mini-halo. Other systems also have diffuse relic emission at the periphery of the cluster (e.g. ACT-CL J0102−4915, also known as El Gordo, has a double radio relic, Lindner et al. 2014; Botteon et al. 2016), and based on the SUMSS images, there might be other sources with possible relic emission (see Section 3.5).

3.4 Systems with possible cavities

McDonald et al. (2013a) have shown that there are cavities in the Phoenix cluster, and Hlavacek-Larrondo et al. (2015) used unsharp-masking techniques to identify possible cavities in seven other SPT clusters. Through visual inspection of the X-ray images, we found evidence for significant structure in 11 systems (see Fig. 1). For these systems, we made unsharp-masked images to make any such structure more evident. Among the CF sample, there are possible cavities in SPT-CL J2106−5845 at $z = 1.132$,[3] which has an S-like enhancement of X-ray emission, possibly due to X-ray cavities which lie along an axis with a small angle to the line of sight (see also NGC4636, Baldi et al. 2009). Alternatively, such an arm-like structure could arise from turbulence driven by core sloshing (Ahoranta et al. 2016). The BCG and X-ray centre are displaced by about 55 kpc (see Fig. 1 and McDonald et al. 2016), and an interesting question is how AGN feedback operates in this case (see

---

[3] SPT-CL J2106−5845 is one of the most X-ray luminous systems in the sample, the fifth most luminous after the Phoenix cluster ($z = 0.595$), El Gordo ($z = 0.87$), AS1063 ($z = 0.351$), and ACT-CL J0438−5444 ($z = 0.421$), and the most massive one above $z > 0.6$.
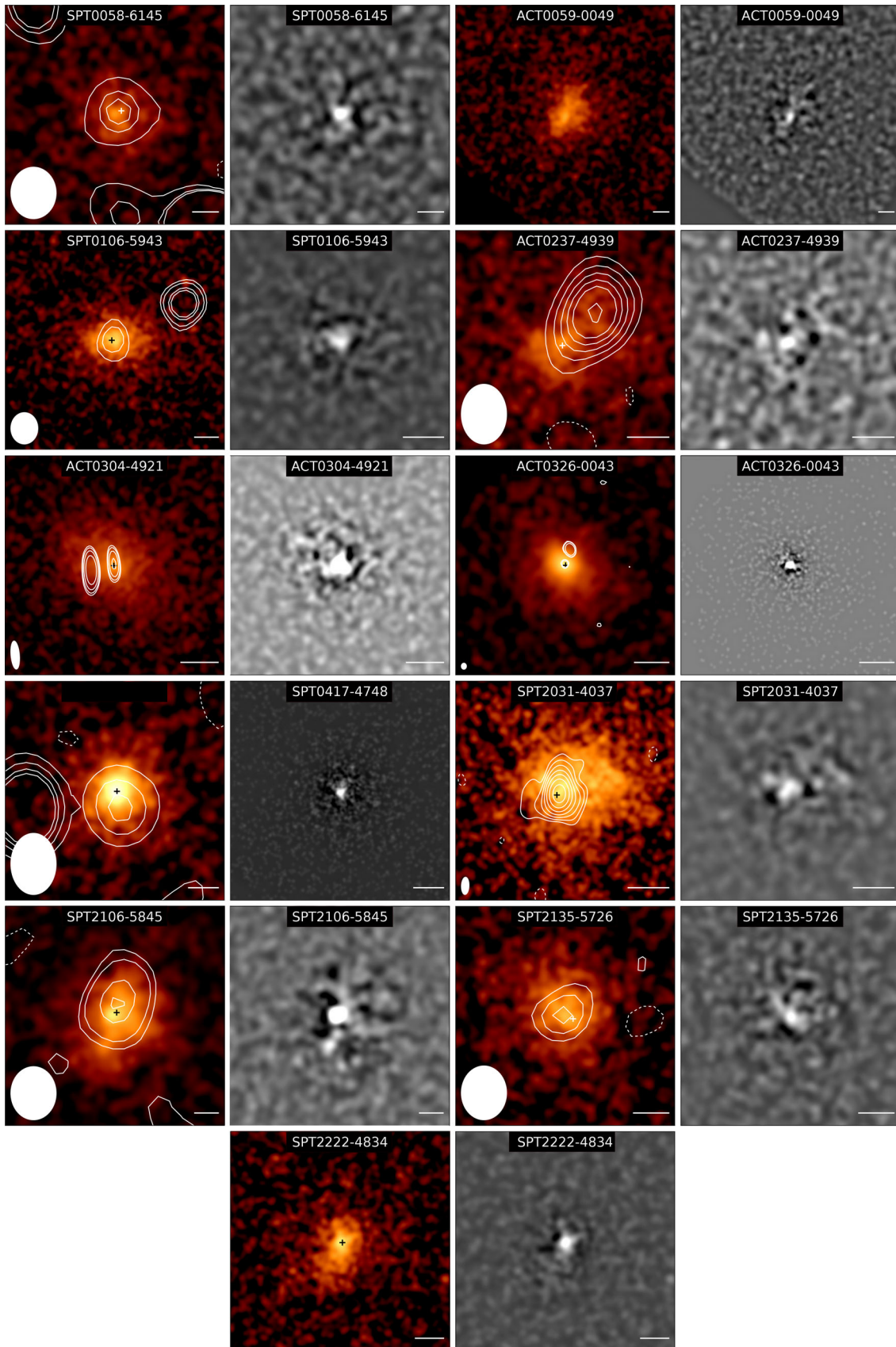
Figure 1. Smoothed and unsharp-masked images for 10 systems which show visible structure in *Chandra* images (see Section 3.4). The radio contours from FIRST (ACT-CL J0326−0043), GMRT (ACT-CL J0304−4921, and SPT-CL J2031−4037), or SUMSS (all others) images are overlaid, and the restoring beam is indicated by the white ellipse in the lower left corner. The BCG location is marked with a cross, and the line in the lower right corner denotes a scale of 200 kpc.
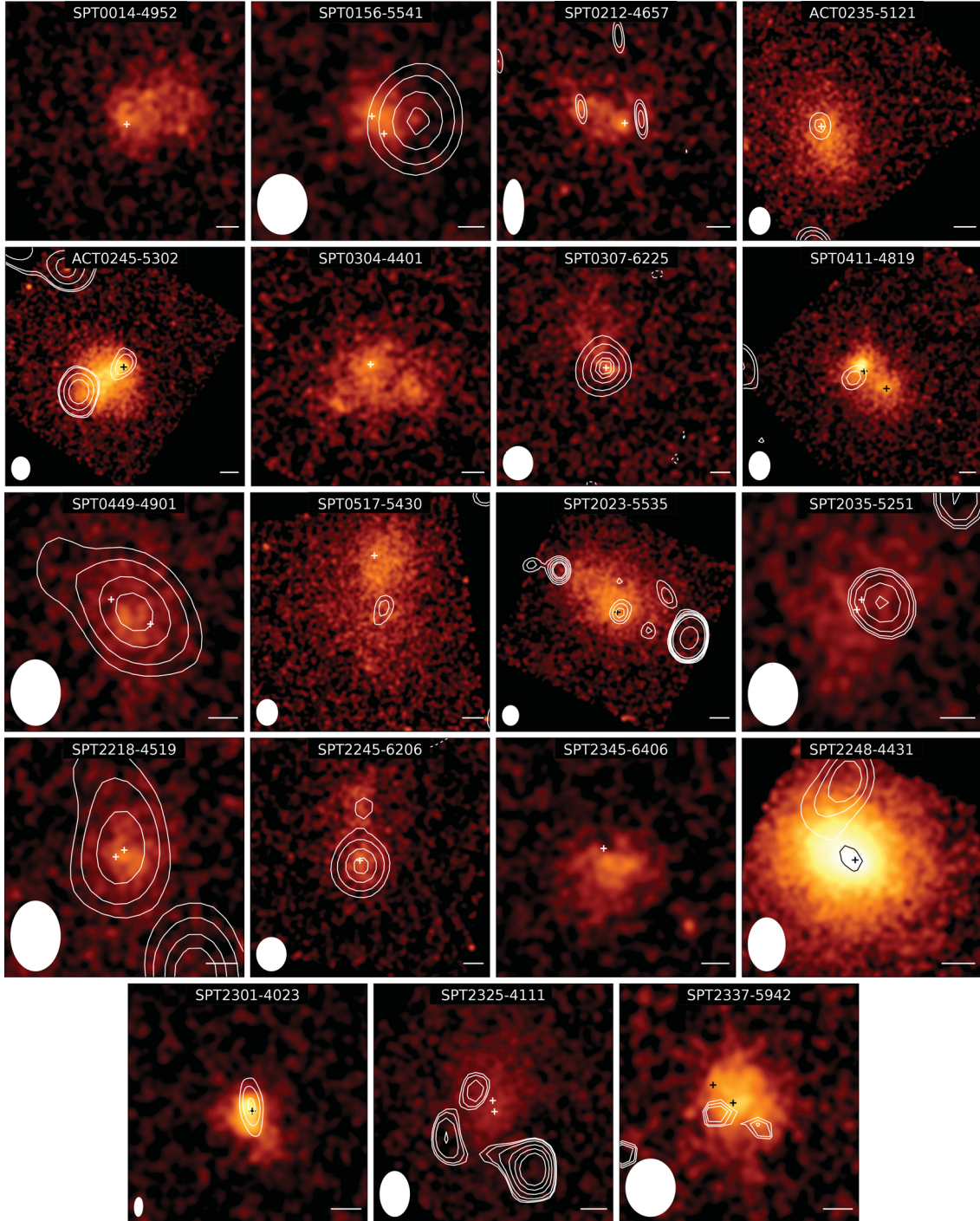
Figure 2. Smoothed *Chandra* images of systems with signs of interactions (see Section 3.5). The radio contours from GMRT (SPT-CL J0212−4657 and SPT-CL J2301−4023) and SUMSS (all others) images are overlaid, and the symbols are the same as in Fig. 1.

Section 4.5).[4] Additionally, there is some evidence for structure in ACT-CL J0304−4921 and SPT-CL J0417−4748. In the case of ACT-CL J0304−4921, we found a lower power cRS in our GMRT image (below the SUMSS detection limit; see Fig. 1). Both

ACT-CL J0304−4921 and SPT-CL J0417−4748 have a radio source displaced from the BCG. However, in these cases, the unsharp-masked images are not consistent with cavities, and as a result the structure we see in the X-ray images might be due to merger activity.

There are also two cavity candidates among the eight intermediate CF systems, SPT-CL J2222−4834 at $z = 0.652$ and SPT-CL J0058−6145 at $z = 0.83$ (see Fig. 1). Additionally, as with SPT-CL J2106−5844, SPT-CL J0058−6145 shows a separation between the X-ray core and the BCG (of ≈ 70 kpc). For both SPT-

---

[4] In the case of SPT-CL J2106−5845, there may also be a separation between the BCG location and radio-source position; however, high-resolution radio observations are needed to verify this.
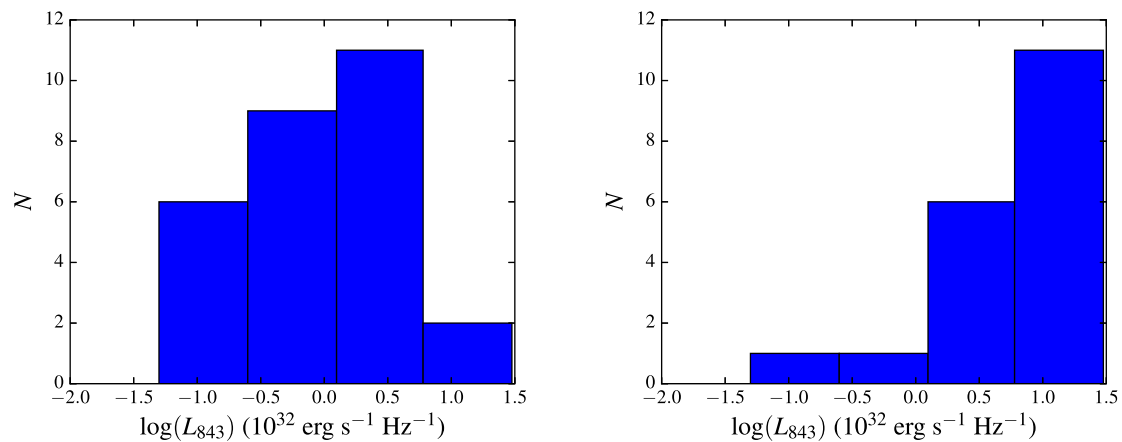
Figure 3. The number of sources with a cRS of a given radio luminosity at 843 MHz for $z < 0.6$ (left-hand panel) and $z > 0.6$ (right-hand panel).

CL J2222−4834 and SPT-CL J0058−6145, the unsharp-masked images support the presence of cavities to the east and west. In the case of SPT-CL J0058−6145, a cRS is also present. There are also cases of possible cavity systems among the NCF systems, e.g. SPT-CL J2135−5722[5] at $z = 0.427$, ACT-CL J0237−4939 at $z = 0.334$, SPT-CL J0106−5943 at $z = 0.348$, and SPT-CL J2031−4037 at $z = 0.342$.

The best cavity system candidate from our sample is SPT-CL J2031−4037, which is one of the NCF systems. In this case, there is also evidence in the GMRT image that the radio emission extends towards the cavity (see Fig. 1). We measure a cavity in this system as an ellipsoid with semimajor and semiminor axes of $9''.3 \times 4''.9$, situated at a projected distance of $18''.3$ from the cluster centre. By assuming that the cavity rose buoyantly from the cluster centre to the current location, we estimate an age of 1.6×10^8 yr and a mechanical power (considering only pV work) of 2.9×10^{44} erg s^{-1} (Bîrzan et al. 2004), enough to balance the X-ray luminosity inside the cooling region (see Table 2). However, the cooling region in the system is small, as only in the very centre does the cooling time drop below 7.7 Gyr.

In summary, there are possible cavities in both CF and NCF systems in our sample. Although we do not expect cavities in NCFs, many of the NCFs might harbour small cool cores (e.g. Sun et al. 2007) that would only be visible in deeper *Chandra* observations (see Section 3.6 for more possible CF candidates).

3.5 Merging activity

Signs of merging activity or interactions are often apparent in X-rays images (e.g. a distorted morphology), radio images (e.g. relic emission), and optical images (e.g. a separation between X-ray and BCG centres). We briefly outline below such evidence in our sample.

In some systems in our sample, the X-ray images show direct evidence of interactions, such as a tail-like structure (e.g. SPT-CL J0307−6225) or the presence of multiple subclusters (see Fig. 2). For example, SPT-CL J0304−4401 shows at least three interacting systems; SPT-CL J0411−4819 shows two interacting systems; SPT-CL J0212−4657 shows an excess of diffuse X-ray emission

at the end of an X-ray tail, perhaps a subgroup, which has its own cRS (there is also radio emission just a little ahead of the cluster core).

Another indicator of merging activity is the relic radio emission, which is thought to be due to cluster–cluster mergers (see the review of Brunetti & Jones 2014). Based on the SUMSS images of our sample, besides the already known relics in El Gordo (Lindner et al. 2014; Botteon et al. 2016), there are possible relics in some other systems (e.g. SPT-CL J2023−5535, which shows evidence of a subcluster on the cluster periphery, see Fig. 2). However, one cannot exclude the possibility that in some of these systems the radio emission may be associated with AGN activity (even if there are no apparent optical counterparts to the radio emission). Deeper optical images and radio images at different frequencies are needed to confirm the putative radio relic emission.

Further evidence of cluster-scale merging activity is the presence of two or more cD galaxies (McDonald et al. 2016). This is the case for SPT-CL J0156−5541 and SPT-CL J0411−4819 (with displaced radio emission, see Fig. 2), among others. Additionally, a large offset between the X-ray core and the BCG location, as seen in El Gordo (for images see Figs 1 and 2), is evidence of significant sloshing, thought to be often triggered by a merger. Evidence of other (e.g. galaxy–galaxy) merging activity is the presence of a nearby companion galaxy to the BCG (McDonald et al. 2016, e.g. SPT-CL J0000−5748) or of asymmetric emission at ultraviolet (UV) wavelengths with a minimum of two peaks.

3.6 X-ray morphology and the central radio source

In Fig. 3, we show the number of detected cRSs as a function of the radio luminosity at 843 MHz. Generally, systems at $z < 0.6$ have lower luminosities than those at $z > 0.6$. This difference is partly due to the flux-limited nature of the radio surveys that we have used (which means that lower luminosity sources cannot be detected at high redshifts), but it is also due to an increased incidence of powerful sources at higher redshifts (see Section 4.2).

For the 20 CF systems with $t_{cool}(10\,kpc) \lesssim 2 \times 10^9$ yr and $t_{cool}/t_{ff} \lesssim 10$, 13 of which have a cRS, the X-ray morphology can be described as small, round, and compact, with a peaked core (with a few exceptions: e.g. the Phoenix cluster, SPT-CL J2106−5845, El Gordo, ACT-CL J0304−4921, SPT-CL J0232−4420*, ACT-CL

---

[5] In the case of SPT-CL J2135−5726, the radio source is displaced from the BCG location, and there is also a separation between the X-ray core and BCG position of 50 kpc.
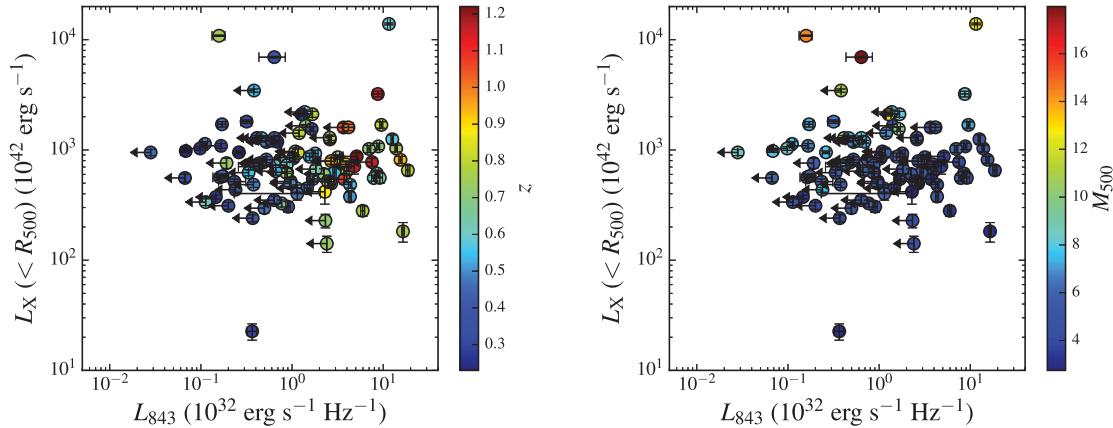
Figure 4. Total bolometric X-ray luminosity inside the R_{500} region, $L_X(<R_{500})$, versus the rest-frame 843 MHz monochromatic radio luminosity for the cRS, L_{843}. The colour denotes the redshift in the left-hand panel and M_{500} in the right-hand panel.

J2129−0005*, SPT-CL J2011−5725*[6]). Only a couple of these systems show evidence for cavities, e.g. the Phoenix cluster (see McDonald et al. 2015). The two systems with $t_{cool}/t_{ff} \lesssim 10$, but $t_{cool}(10 \, kpc) > 2 \times 10^9$ yr are large, bright, and elongated, e.g. SPT-CL J2248−4431 (see Fig. 2).

The four systems with $t_{cool}(10 \, kpc) > 2 \times 10^9$ yr, but $\eta_{min} \lesssim 10$ (see Section 3.2) do not have a cRS above the detection limit (see Table 2). For the eight intermediate systems, with $t_{cool}(10 \, kpc) \lesssim 2 \times 10^9$ yr and $t_{cool}/t_{ff} > 10$, only two have a cRS, and both have a significant separation between the X-ray peak and BCG location (see Section 3.5). However, some of these have low central temperatures and peaked SB profiles and hence might be classified as CF systems in deeper *Chandra* observations (e.g. SPT-CL J2352−4657).

Of the remaining 65 NCF systems, 32 have a cRS. The NCF systems have a variety of X-ray morphologies, but mostly they can be described as disturbed and often show evidence of merging activity, such as two BCGs (e.g. SPT-CL J2035−5251 and SPT-CL J2337−5942, see Fig. 2), sharp edges (e.g. SPT-CL J2258−4044 and SPT-CL J2233−5339), or an elongated tail-like appearance (e.g. ACT-CL J0235−5121, see Fig. 2).

Notably, in contrast to local samples (e.g. the B55 sample), some of the NCFs in our sample host powerful cRSs (up to $L_{843} \sim 1.9 \times 10^{33}$ erg s^{-1} Hz^{-1}). Presumably, this radio activity is unrelated to feedback but is instead triggered by other factors. Additionally, this difference points to evolution in the cRSs in NCFs, and we discuss this possibility further in Section 4.2.

3.7 Star formation rates

We use the SFRs of McDonald et al. (2016), who computed SFRs from UV, O II, and infrared (IR) data. The data used in McDonald et al. (2016) to calculate the SFRs comes from photometric-redshift follow-up campaigns (Song et al. 2012; Bleem et al. 2015) plus *U*-band imaging from McLeod et al. (2015). Of the three SFRs listed in McDonald et al. (2016), we use the IR-derived SFR, unless one of the other values was a detection and the IR-derived SFR was only an upper limit or when there was no IR-derived SFR listed for that system. If a system had two or more detections, we use the average of the detected rates as the SFR for that system. The SFRs are given in Table 2.

[6] The systems with an asterisk were detected in one or more X-ray surveys and are at $z \approx 0.3$ (see Table 2).

4 RESULTS AND DISCUSSIONS

4.1 X-ray versus radio luminosity

In Fig. 4, we plot the bolometric X-ray luminosity inside the R_{500} region, $L_X(<R_{500})$, versus the rest-frame 843 MHz monochromatic radio luminosity for the cRS, L_{843}. The highest monochromatic radio luminosity in our sample is $L_{843} \sim 1.9 \times 10^{33}$ erg s^{-1} Hz^{-1} for SPT-CL J0449−4901 at a redshift of $z = 0.79$, one of the systems with two BCGs (see Table 2 and Fig. 2). Based on the X-ray data, this system was classified as an NCF (see Table 1). Overall, the range in radio luminosity at 1400 MHz (extrapolated from 843 MHz assuming $\alpha = 1.0$) is $L_{1400} \sim 0.04–10 \times 10^{32}$ erg s^{-1} Hz^{-1}. This range is considerably smaller than that of the B55 and HIFLUGCS samples, where the 1400 MHz luminosity ranges from 10^{28} to 10^{35} erg s^{-1} Hz^{-1} (Bîrzan et al. 2012). Additionally, the lower limit of this range is above the threshold that separates CFs and NCFs in local samples of $L_{1400} \sim 2.5 \times 10^{30}$ erg s^{-1} Hz^{-1} (see Bîrzan et al. 2012). However, since we mainly used shallow survey data (e.g. SUMSS, Mauch et al. 2003), the sensitivity of our radio data is generally insufficient to detect the low-luminosity sources.

Furthermore, in our sample, there are no cRSs with $L_{843} > 10^{34}$ erg s^{-1} Hz^{-1}, such as those that appear in local X-ray flux-limited cluster samples (e.g. Cygnus A). This lack can be partly explained by the radio-luminosity bias of SZ surveys (Lin et al. 2015), which tends to select against such sources, and by the fact that such luminous sources are rarely found in massive clusters (of which the SZ samples are predominantly comprised).

However, our sample does have a number of powerful radio sources, with luminosities above the canonical FRI–FRII dividing line. The commonly used luminosity separation between FRI and FRII sources (Fanaroff & Riley 1974) corresponds to $L_{178} \sim 2 \times 10^{32}$ erg s^{-1} Hz^{-1} Sr^{-1} at the rest-frame frequency of 178 MHz, or $L_{1400} \sim 10^{31.5}$ erg s^{-1} Hz^{-1} Sr^{-1} at 1.4 GHz (which corresponds to a monochromatic luminosity at 843 MHz of $L_{843} \sim 5 \times 10^{32}$ erg s^{-1} Hz^{-1}, assuming a spectral index of $\alpha = 1.0$). The more powerful FRII sources are found to preferentially avoid clusters at lower redshifts (Owen & White 1991) and be present in rich clusters around $z = 0.5$ or higher (Yee & Green 1987; Hill & Lilly 1991; Belsole et al. 2007). Morphologically, FRI sources show two-sided jet-dominated emission that smoothly extends into the ICM and at kpc scales forms large-scale lobes of diffuse radio emission, whereas FRII sources have lobe-dominated

emission with collimated jets on kpc scale that terminate in hotspots.[7]

There is a large overlap between sources classified as FRI/FRII and those classified as LERG/HERG (Evans et al. 2006; Hardcastle et al. 2007; Best & Heckman 2012; Heckman & Best 2014; Mingo et al. 2014), although some FRIs are high-excitation radio galaxies (HERGs; e.g. Perseus, M87) and some FRIIs are LERGs (Gendre et al. 2013). Recently, Turner & Shabala (2015) developed a model which incorporated both FRII (Kaiser & Alexander 1997) and FRI models (Luo & Sadler 2010) and supports the conclusion that differences between LERGs and HERGs is due to differences in the accretion mechanism.

Using a monochromatic luminosity of $L_{843} \sim 5 \times 10^{32}$ erg s^{-1} Hz^{-1} to classify our sources as FRI or FRII, we find that in our sample there are 15 sources with FRII-like radio power (see Table 2 and Fig. 4). Because of the large beam size of SUMSS images of $\approx 40''$ (Mauch et al. 2003), the cRSs in our sample are mostly unresolved and we cannot therefore distinguish between FRI or FRII sources based on their radio morphology. The only clear case when the cRS is resolved is in SPT-CL J0542−4100 (or RDCS J0542−4100 at $z = 0.64$), where the central source is ∼600 kpc across, but the image is inconclusive.

All of the high-power sources are also higher redshift sources ($z \gtrsim 0.6$). Four of them are hosted by clusters classified as CFs (the Phoenix cluster, SPT-CL J2106−5845, SPT-CL J0000−5748, and ACT-CL J0616−5227), all of which have possible cavities (this paper and Hlavacek-Larrondo et al. 2015; McDonald et al. 2015). The remaining 11 high-power sources are in clusters classified as NCFs, some of which show signs of merging activity (e.g. SPT-CL J2245−6206, SPT-CL J0449−4901, and SPT-CL J2218−4519, see Fig. 2). We will discuss the relation between the cluster state and the radio properties in more detail in Section 4.3.

Fig. 4 (*left*) shows that the higher redshift sources ($z > 0.6$) have on average higher radio luminosity than lower redshift sources. As we noted above, all the FRII-like cRSs are at $z \gtrsim 0.6$, and there are only few sources with high radio luminosity, $L_{843} > 2.7 \times 10^{32}$ erg s^{-1} Hz^{-1}, at lower redshift, $z < 0.6$. This is the case for SPT-CL J2344−4242 (the Phoenix cluster) at $z = 0.595$ and SPT-CL J2245−6207 at $z = 0.58$ (with a radio luminosity above 10^{33} erg s^{-1} Hz^{-1}, they are part of the 15 most powerful radio sources discussed above), ACT-CL J0215−5212 at $z = 0.48$, SPT-CL J0456−5116 at $z = 0.562$ with a radio luminosity above 4×10^{32} erg s^{-1} Hz^{-1}, and ACT-CL J0346−5438 at $z = 0.53$, SPT-CL J0307−6225 at $z = 0.59$, and SPT-CL J0234−5831 at $z = 0.415$ with a radio luminosity above 2.7×10^{33} erg s^{-1} Hz^{-1}.

An explanation for the higher radio luminosity in the higher redshift systems might be that, due to the fact that these systems tend to be younger and less relaxed than similar systems at lower redshift, there is more merging activity that contributes to the triggering of the radio activity (see Section 4.2 and Branchesi et al. 2006). This increase of the merging activity with redshift is also supported by the commensurate increase in the SFRs at higher redshift (see Section 4.4 and McDonald et al. 2016).
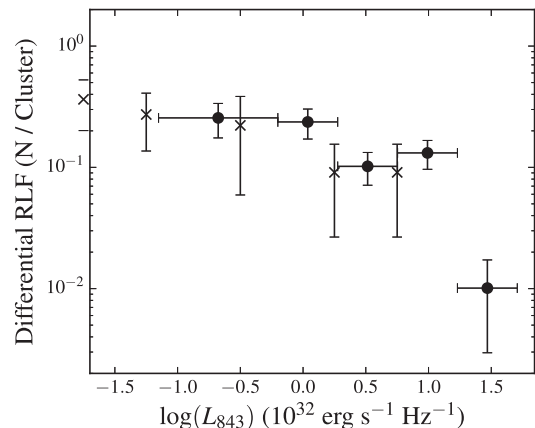
Figure 5. The differential RLF at 843 MHz for our SPT sample (filled circles) and the sample of Branchesi et al. (2006) of $0.3 < z < 0.8$ X-ray-selected NEP clusters (crosses), adjusted for our method of calculating the RLF.

4.2 Radio-luminosity functions

The radio-luminosity function (RLF) encapsulates the fraction of sources in a sample that possess a radio source of a given luminosity, and as such is a sensitive tool for detecting evolutionary effects in the radio properties (e.g. Branchesi et al. 2006; Pracy et al. 2016). In this work, as we are interested only in the central source (that responsible for feedback), we calculate the differential RLF for only the radio source associated with the BCG that lies at the X-ray core, in contrast to, e.g. Ledlow & Owen (1996) and Branchesi et al. (2006) who calculate it for all radio sources within a distance $R < 0.2R_A$, where R_A is the Abell radius. Therefore, our RLF may be interpreted as being the number of cRSs per cluster per luminosity bin.

We calculate the RLF following the approach of Branchesi et al. (2006). For each of the 44 clusters with a detected cRS, we calculate its contribution to the RLF as:

$$W_{\mathrm{RLF},i} = 1/N_{\mathrm{cl},i}, \tag{3}$$

where $W_{\mathrm{RLF},i}$ is the contribution of source i and $N_{\mathrm{cl},i}$ is the number of clusters in which source i could have been detected, given its peak flux density and the sensitivity limit of the radio observations (see Section 3.3 for details of the radio data). As in Branchesi et al. (2006), we adjust the bin size of the lowest luminosity bin so that all bins contain at least two sources, and we scale the normalization of this bin so that it matches the other bins (which have a size of 0.5 dex). Furthermore, to allow a direct comparison between the results of Branchesi et al. (2006) and our results, we recalculated the RLF of Branchesi et al. (2006) using our method of considering only the cRS, rather than all sources within $R/R_A < 0.2$.

In Fig. 5, we plot the RLF at 843 MHz for our sample and that of Branchesi et al. (2006). The Branchesi et al. (2006) sample of 18 clusters was constructed by selecting all clusters with $z > 0.3$ from the *ROSAT* North Ecliptic Pole (NEP) catalogue of Gioia et al. (2003). Our results agree fairly well with those of Branchesi et al. (2006) over the range of luminosities for which there is overlap. Branchesi et al. (2006) found that their RLF did not possess the high-luminosity break seen in local RLFs (e.g. Ledlow & Owen 1996; Sadler et al. 2002; Best et al. 2005; Mauch & Sadler 2007). In contrast, we do see evidence for a break around a luminosity of $L_{843} \approx 10^{33}$ erg s^{-1} Hz^{-1}, considerably above the highest luminosity probed by Branchesi et al. (2006) and higher than the break

---

[7] Recently, a new class was introduced to describe the radio sources which lack extended emission (FR0, Sadler et al. 2014; Baldi, Capetti & Giovannini 2015).
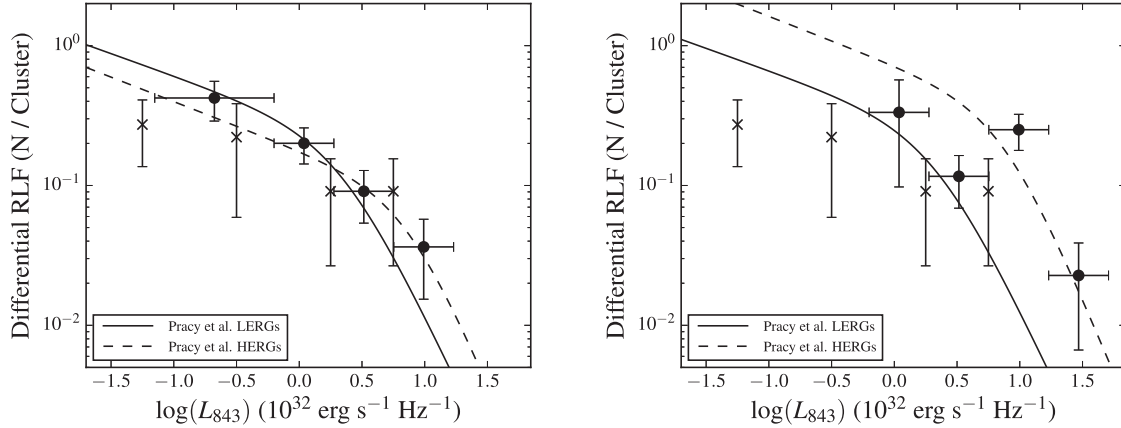
Figure 6. The differential RLF for $z < 0.6$ SPT clusters (*left*) and $z > 0.6$ SPT clusters (*right*). Symbols are the same as those in Fig. 5. The lines show the RLFs of Pracy et al. (2016) for LERGS (*solid lines*) and HERGs (*dashed lines*), calculated with the median redshift of the sample and normalized so that the low-z LERG relation matches the value of the SPT-ACT RLF in the lowest luminosity bin.

luminosity seen in local RLFs of $L_{843} \approx 10^{32}$ erg s^{-1} Hz^{-1} (after converting from 1400 MHz to 843 MHz; Ledlow & Owen 1996).

To better understand the origin of this break, we plot in Fig. 6, the RLF in two redshift ranges ($z < 0.6$ and $z > 0.6$). For comparison to the overall population of radio sources, we plot the parametrizations of the RLFs determined by Pracy et al. (2016) for LERGs and HERGs for pure luminosity evolution, calculated for the median redshifts of the two samples. To account for the different normalizations between our RLF and that of Pracy et al. (2016), we normalize the relation of Pracy et al. (2016) so that their LERG relation matches the value in the lowest luminosity bin of our $z < 0.6$ sample.[8] We choose this point for the normalization because the systems in this luminosity bin should be comprised almost entirely of LERGs (alternatively, we could use the highest luminosity bin for the normalization and normalize the HERG relation to fit it instead of the LERG one, but this would give a similar value). We use a single normalization factor across all four relations (low- and high-redshift LERGs and HERGs) and calculate the relations using the median redshift of each sample. One can see from the lower redshift plot of Fig. 6 that the lower luminosity bins of our RLF follow the LERG relation well, while the higher luminosity ones match the HERG relation well, suggesting that there is a transition between the two source types that blurs the break seen in local samples (e.g. Ledlow & Owen 1996).

At higher redshifts ($z > 0.6$), shown in Fig. 6 (right), we see further support for this LERG–HERG dichotomy and evidence for strong evolution in the HERG population. At these redshifts, the fraction of clusters with a cRS in the $L_{843} \approx 10^{33}$ erg s^{-1} Hz^{-1} bin is a factor of ≈ 7 larger than the fraction in the same bin at lower redshifts, a $\approx 3\sigma$ difference. Furthermore, the RLF in the highest luminosity bins match well the expected values from the HERG relation of Pracy et al. (2016), calculated for the median redshift of the sources in our sample at $z > 0.6$. Therefore, it appears that the RLF of the central BCG agrees with that of the overall radio-source population in the same redshift range (see Dunlop & Peacock 1990; Willott et al. 2001; Grimes, Rawlings & Willott 2004; Sadler et al. 2007; Best & Heckman 2012; Best et al. 2014; Pracy et al. 2016), perhaps because powerful, RL sources in general tend to be located

in cluster cores (see Hill & Lilly 1991; Mandelbaum et al. 2009; Wylezalek et al. 2013).

Therefore, the more powerful sources in our sample, which appear preferentially at higher redshifts, are consistent with being HERGs. Merging may play an important role in triggering these HERGs, as many of the high-redshift systems show signs of recent minor mergers in both the SPT sample (McDonald et al. 2016), and the NEP sample (Branchesi et al. 2006). Additionally, it might be that minor mergers are more effective in coupling the AGN to the cold gas than in the local universe (Kaviraj et al. 2015; Shabala et al. 2017).

4.3 Cooling time/thermal stability parameters and radio luminosity

In Figs 7 and 8, we plot the central cooling time at 10 kpc (Fig. 7, left-hand panel), the ratio of central cooling time versus the free-fall time (Fig. 7, right-hand panel) and the minimum instability criterium (Fig. 8) versus the monochromatic 843 MHz radio luminosity (see Table 1). In the cases for which the central cooling time extrapolation did not work (e.g. the SB profile is too noisy or there is significant substructure that is inconsistent with the deprojection method, see Section 3.2), we plot the cooling time of the inner bin derived from the deprojection. As expected from the mostly flux-limited nature of the radio data, the lower luminosity half of the plots is dominated by the lower redshift systems ($z < 0.6$) and the higher luminosity half by the higher redshift systems ($z > 0.6$).

The sampled radio luminosities cover only part of the range sampled by the B55 and HIFLUGS samples (Bîrzan et al. 2012), since, due to the generally higher redshifts and lower sensitivity of the radio data (e.g. SUMSS), we cannot probe the behaviour of the lower luminosity sources in our sample.[9] Therefore, our sample only probes radio luminosities above the threshold seen by Bîrzan et al. (2012) for NCFs of $L_{843} \sim 4 \times 10^{30}$ erg s^{-1} Hz^{-1} (see Section 4.1). Strikingly, in contrast to nearby samples (Bîrzan et al. 2012), there is no apparent difference in the distribution of radio luminosities between CF and NCF systems above this threshold. The reason for

---

[8] A single normalization is appropriate, since the per-source volume and magnitude weights used in Pracy et al. (2016) are constant across our (volume-limited) sample (see e.g. Yuan et al. 2016).

[9] In the B55/HIFLUGCS samples, we found that the lower luminosity systems tend to be found in NCFs and lower mass systems (ellipticals and groups).
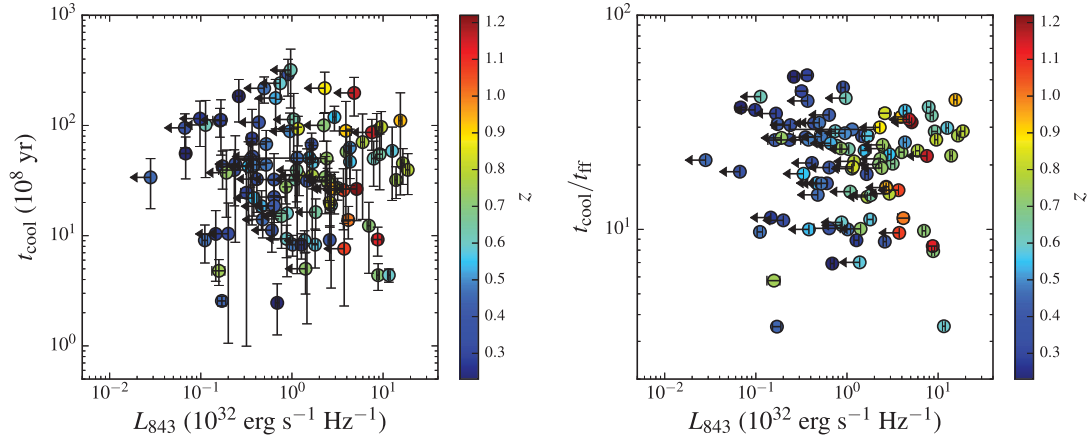
Figure 7. *Left*: central cooling time (at 10 kpc) versus the rest-frame monochromatic 843 MHz radio luminosity. *Right*: the ratio of central cooling time and free-fall time versus the radio luminosity. The colour indicates the redshift in both panels.
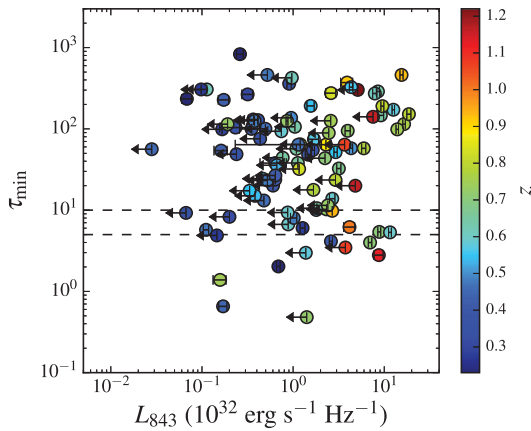

Figure 8. Thermal-stability parameter versus the rest-frame monochromatic 843 MHz radio luminosity. The colour indicates the redshift. The lines denote values of 5 and 10.

this is the presence of powerful radio sources in the NCFs in our sample, which are generally lacking in local samples.

4.4 Thermal stability and star formation

Fig. 9 shows the thermal-stability parameter (the cooling time versus the free-fall time) versus the SFR. There is no clear thermal-stability threshold below which SF occurs, as is seen in nearby systems (Rafferty et al. 2008; Voit et al. 2008). However, the CF systems tend to have higher SFR rates in general (SFR > 20 $M_\odot$ yr^{-1}). Additionally, systems with higher SFRs tend to lie at higher redshift.

The systems with the highest SFRs are found both in CF systems (e.g. the Phoenix cluster, SPT-CL J2106−5845, and SPT-CL J2043−5035) and NCF systems (e.g. SPT-CL J0446−5849, SPT-CL J2345−6406, and SPT-CL J0547−5345), and as the left-hand panel of Fig. 9 shows, they are some of the highest redshift systems. For example, the highest SFRs in NCF systems are in SPT-CL J0446−5849 at $z = 1.16$ and SPT-CL J2345−6406 at $z = 0.94$. SPT-CL J2345−6406 shows some structure in the X-ray image (see Fig. 2), which could be due either to cavities or merging activity; and the lower central temperature ($kT \sim 4$) and peaked SB are indications that some of these high-redshift systems with high SFRs might be in a cooling stage. but lack sufficient counts to be securely detected as a cool core (see also Section 4.3). In a similar situation

are SPT-CL J0534−5005 at $z = 0.881$ and SPT-CL J2236−4555 at $z = 1.16$.

The main question that arises from Fig. 9 is why we do not see the SFR threshold as in nearby samples. A possible explanation is that the systems with high SFRs do have shorter cooling times, but the X-ray data were insufficient to detect them. However, among the most likely such systems (see Sections 3.6 and 4.3), only a few have detections of SFR > 20 $M_\odot$ yr^{-1} (e.g. SPT-CL J0509−5342 and SPT-CL J0058−6145). Additionally, it is possible that minor mergers are more common at higher redshifts and these trigger bursts of SF (McDonald et al. 2016). Between the systems with detected high SFRs and possible evidence of interactions are SPT-CL J0547−5345 at $z = 1.067$, SPT-CL J0406−4804 at $z = 0.737$, and SPT-CL J2035−5251 at $z = 0.424$ (see Fig. 2).

Additionally, in right-hand panel of Fig. 9, there is no clear dependence of the SFR or cooling state on the radio luminosity. For example, the highest luminosity systems are distributed fairly randomly and appear in both CFs (e.g. SPT-CL J2106−5845, SPT-CL J0000−5748, and SPT-CL J2344−4242) and NCFs (e.g. SPT-CL J0449−4901 with two BCGs, see Fig. 2, and SPT-CL J0058−6145, with possible cavities, see Fig. 1). Interestingly, a few of the strongest CF clusters have the highest SFRs in our sample and harbour some of the most powerful cRSs (e.g. the Phoenix cluster and SPT-CL J2106−5845).

4.5 Quenching cooling

For systems with visible cavities in *Chandra* images, it was found that AGN heating is sufficient to balance cooling losses from the X-ray emitting gas within the cooling radius in at least 50 per cent of the systems (Rafferty et al. 2006). This sample was mostly composed of nearby systems, but 10 out of a total of 33 systems were at $z > 0.1$ (the highest at $z = 0.545$). Furthermore, Hlavacek-Larrondo et al. (2012) increased the number of higher redshift ($0.3 < z < 0.5$) sources using the MACS luminous cluster sample and found that, as in nearby cluster samples, AGN feedback supplies enough energy to balance the cooling in the inner regions of the cluster. To investigate whether AGN feedback is enough to balance cooling out to a redshift $z = 1.2$, we use the monochromatic radio luminosity to estimate a cavity power using the radio-to-jet power scaling relations of Cavagnolo et al. (2010). We adopt a spectral index of $\alpha = 1.0$ to transform our 843 MHz radio powers to 1400 MHz powers.
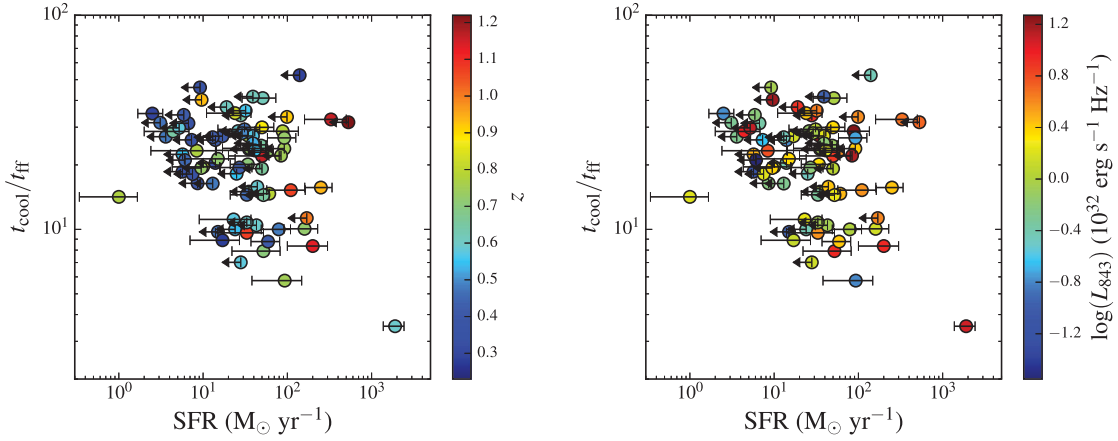
Figure 9. The ratio of cooling time and free-fall time versus the SFR. The colour represents the redshift (*left*) and radio luminosity (*right*).
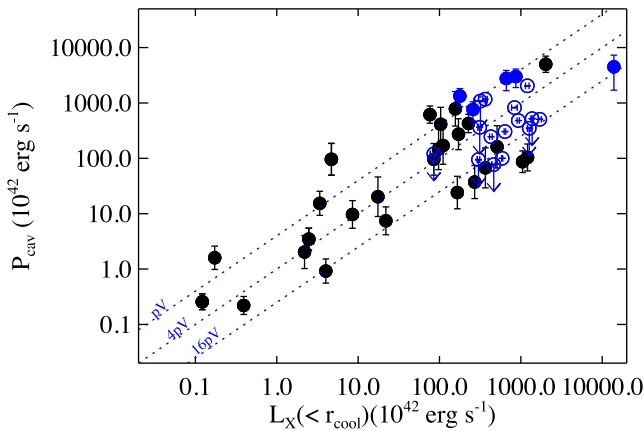
Figure 10. Cavity power of the central AGN versus the X-ray luminosity of the ICM inside the cooling region. The filled symbols are the measured cavity power from the HIFLUGCS sample (*black* symbols, Bîrzan et al. 2012) and SPT sample (*blue* symbols, Hlavacek-Larrondo et al. 2015; McDonald et al. 2015), and the open symbols are the estimated cavity power using the scaling relations between monochromatic 1.4 GHz radio luminosity and the cavity power of Cavagnolo et al. (2010). The diagonal lines indicate $P_{cav} = L_X$ assuming pV, $4pV$ or $16pV$ as the energy deposited.

The Cavagnolo et al. (2010) relation is an extension of the Bîrzan et al. (2008) relation, with the addition of 21 nearby elliptical systems from Nulsen et al. (2009) at the lower luminosity end, and is given by:

$$\log(P_{cav}) = 1.91 + 0.75 \times \log(L_{1400}),\qquad(4)$$

where P_{cav} is in units of 10^{42} erg s^{-1}, and L_{1400} in units of 10^{40} erg s^{-1} ($\approx 10^{24}$ W Hz^{-1}). We plot in Fig. 10, the measured or predicted cavity power versus the total X-ray luminosity of the intracluster gas within the cooling radius (see Section 3) for the 20 CF systems in our sample. For comparison with previous results from the nearby universe, these predicted values are overplotted with the measured values from the HIFLUGCS sample (see Fig. 10 and Bîrzan et al. 2012). In general, the measured and predicted jet powers are sufficient to balance cooling in $\approx$50 per cent of the high-redshift CF systems in our sample, similar to local samples (Bîrzan et al. 2012).

We also investigated the radio-to-jet power scaling relation of Godfrey & Shabala (2016). This relation was computed using a multivariant regression between cavity power (P_{cav}), radio luminosity at 1.4 GHz (L_{1400}), and distance (D_L) using combined

cavity samples of Bîrzan et al. (2008), Cavagnolo et al. (2010), and O'Sullivan et al. (2011). Generally, it predicts more jet power at low radio luminosities and less jet power at higher luminosities. For our sample, the predicted jet powers from this relation are a factor of $\sim$6–8 times less than those predicted by the relation of Cavagnolo et al. (2010) or measured directly (Hlavacek-Larrondo et al. 2015; McDonald et al. 2015, and this paper).

As pointed out by Godfrey & Shabala (2016), both the scaling relations of Cavagnolo et al. (2010) and Godfrey & Shabala (2016) are inconsistent with models of radio-source evolution: one expects a slope of 0.5 from buoyancy arguments and a slope of 0.8 from FRII expansion models (Willott et al. 1999; Ineson et al. 2017). However, Bîrzan et al. (2008) found that accounting for the effects of spectral aging on the observed radio luminosity gives a slope of $\sim$0.5, bringing the observed scaling between jet power and radio luminosity into agreement with the buoyancy models. Basically, these aging effects result in a steepening of the relation, as lower luminosity sources tend to have more spectral aging than the higher luminosity sources.[10]

5 SUMMARY AND DISCUSSION

In this paper, we use a large sample of SZ-selected clusters from the Southern hemisphere and galactic plane (the SPT and ACT samples) to investigate AGN feedback to high redshift (0.3 < z < 1.2). To identify the CF systems in our sample, we use the instability criterion whereby systems with $t_{cool}/t_{ff} \lesssim 10$ are considered unstable to cooling (resulting in 22 CF systems; see Section 3.6 for a description of these systems). In this case, the instability criterion of 10 corresponds roughly to a inner cooling time of 2×10^9 yr (with two exceptions, see Section 3.2), but not all the systems with t_{cool}(inner) $\lesssim 2 \times 10^9$ yr have $t_{cool}/t_{ff} \lesssim 10$ (these are the intermediate systems described in Section 3.6). The reason for such a high cooling time value for the separation between CF systems and NCF systems is the fact that for such a high-redshift sample we are not able to probe

---

[10] The monochromatic scaling relations at lower frequencies, such as at 327 MHz (Bîrzan et al. 2008) or 140 MHz (Kokotanekov et al., 2017) also have a slope of $\sim$0.5. Although low-frequency observations are generally less sensitive to spectral aging effects than higher frequency observations, they still suffer from the overall dimming of the radio emission. In order to account for the effects of this dimming and the spectral shape on the scaling relations, information on the spectral age (e.g. the break frequency) is required.

the densest gas close to the core. As a result, the separation based on cooling time does not work as well as for the nearby systems (see the left-hand panel of Fig. 7).

We investigate whether the locally derived scaling relation between cavity power and radio luminosity (e.g. Bîrzan et al. 2004) holds at higher redshifts. Direct measurement of AGN feedback power through cavities is possible for only few systems in our sample, e.g. the Phoenix cluster (McDonald et al. 2013a) and SPT-CL J2031−4037 (this paper, see Section 3.4). There is evidence of X-ray structure in some other systems, which might be due to cavities (e.g. SPT-CL J2135−5726, SPT-CL J2222−4834, among many others, see Fig. 1 and Section 3.4), but because of the shallow nature of the X-ray and radio data, many of these potential X-ray cavities are uncertain. We therefore use radio data from the SUMSS survey (Bock et al. 1999) and SFRs from McDonald et al. (2016), in addition to the *Chandra* X-ray data, to investigate AGN feedback. As discussed in the Introduction, the SFR is an important ingredient in the feedback process and traces the imperfect balance between heating and cooling (see the discussion in Voit et al. 2016).

Below we summarize our main results:

(i) We find evidence in the RLF of the cRS, calculated at 843 MHz, for strong evolution in the higher luminosity sources, such that the fraction of sources hosting a cRS of $L_{843} \sim 10^{33}$ erg s^{-1} Hz^{-1} is ≈7 times higher in our sample of $z > 0.6$ sources than in the $z < 0.6$ sources. This evolution is consistent with other studies (e.g. Pracy et al. 2016) of the general galaxy population that find that high-power HERGs are much more common at high redshifts than at lower redshifts. We argue that the underlying cause of the break is therefore the same as that in the general population, namely it is due to differences of the accretion mechanism on to the SMBH in the low- and high-luminosity sources (Best et al. 2014; Mingo et al. 2014; Fernandes et al. 2015). We postulate that mergers likely have an important influence on this accretion mechanism (see also Hardcastle et al. 2007; Ramos Almeida et al. 2012), since many of the high-redshift systems appear to be going through minor mergers (McDonald et al. 2016), and minor mergers are thought to be more effective in coupling the AGN to the cold gas than in the local universe (Kaviraj et al. 2015; Shabala et al. 2017).

In support of this scenario, we found that there are 15 sources with FRII-like radio power in our sample (see Fig. 4), all of which lie at $z > 0.6$ and many of which are located in likely NCF clusters, which generally show increased merging activity compared to CF clusters. Furthermore, the increased SFRs at higher redshifts seen in our sample (see Section 4.4 and McDonald et al. 2016) are consistent with a commensurate increase in the merging activity.

(ii) We do not find a clear separation between CF and NCF systems based on the radio luminosity or SFR as is observed in the nearby universe, where NCF systems tend to have low radio luminosities (Sun 2009; Bîrzan et al. 2012) and little to no SF (Rafferty et al. 2008; Cavagnolo et al. 2008; Voit et al. 2008). However, the CF systems in our sample do tend to have higher SFRs in general than the NCF systems (SFR > 20 M$_\odot$ yr^{-1}).

(iii) We find that the predicted degree to which AGN feedback can balance the cooling losses in our sample depends on the relation used to transform from radio luminosity to jet power, with the relation of Cavagnolo et al. (2010) implying that the high-redshift CF systems from SPT/ACT sample have enough energy power to balance cooling, and the relation of Godfrey & Shabala (2016) implying that these high-redshift systems have at least four times too little energy to balance cooling. However, the few direct measurements of cavities that exist for our sample (e.g. the Phoenix cluster, McDonald et al. 2015) agree with the values predicted by the Cavagnolo et al. (2010) relation. Further cavity measurements in these systems are required to determine which relation is the more correct one.

Additionally, many of these high-redshift systems are luminous radio sources, lying at the transition between FRI and FRII sources. Furthermore, McDonald et al. (2015) shows that the Phoenix cluster lies at the transition between radio- and quasar-mode AGN activity (Churazov et al. 2005; Russell et al. 2013; Hlavacek-Larrondo et al. 2013). Therefore, we cannot exclude the possibility that, for these powerful radio sources, one needs to use a different radio-to-jet power relation (e.g. the FRII relation with a slope of 0.8; Willott et al. 1999). In particular, a relation that includes spectral information, such as that derived by Bîrzan et al. (2008), would help to mitigate the effects of inhomogeneous radio-source populations and spectral aging on the predicted jet power.

REFERENCES

Ahoranta J., Finoguenov A., Pinto C., Sanders J., Kaastra J., de Plaa J., Fabian A., 2016, A&A, 592, A145
Antognini J., Bird J., Martini P., 2012, ApJ, 756, 116
Baldi A., Forman W., Jones C., Kraft R., Nulsen P., Churazov E., David L., Giacintucci S., 2009, ApJ, 707, 1034
Baldi R. D., Capetti A., Giovannini G., 2015, A&A, 576, A38
Banerjee N., Sharma P., 2014, MNRAS, 443, 687
Belsole E., Worrall D. M., Hardcastle M. J., Croston J. H., 2007, MNRAS, 381, 1109
Best P. N., Heckman T. M., 2012, MNRAS, 421, 1569
Best P. N., Kauffmann G., Heckman T. M., Brinchmann J., Charlot S., Ivezić Ž., White S. D. M., 2005, MNRAS, 362, 25
Best P. N., Kaiser C. R., Heckman T. M., Kauffmann G., 2006, MNRAS, 368, L67
Best P. N., Ker L. M., Simpson C., Rigby E. E., Sabater J., 2014, MNRAS, 445, 955
Bîrzan L., Rafferty D. A., McNamara B. R., Wise M. W., Nulsen P. E. J., 2004, ApJ, 607, 800
Bîrzan L., McNamara B. R., Nulsen P. E. J., Carilli C. L., Wise M. W., 2008, ApJ, 686, 859
Bîrzan L., Rafferty D. A., Nulsen P. E. J., McNamara B. R., Röttgering H. J. A., Wise M. W., Mittal R., 2012, MNRAS, 427, 3468
Blanton E. L., Sarazin C. L., McNamara B. R., Wise M. W., 2001, ApJ, 558, L15
Bleem L. E. et al., 2015, ApJS, 216, 27
Bock D., Large M. I., Sadler E. M., 1999, AJ, 117, 1578
Böhringer H. et al., 2004, A&A, 425, 367
Botteon A., Gastaldello F., Brunetti G., Kale R., 2016, MNRAS, 463, 1534
Branchesi M., Gioia I. M., Fanti C., Fanti R., Perley R., 2006, A&A, 446, 97
Brighenti F., Mathews W. G., Temi P., 2015, ApJ, 802, 118
Brunetti G., Jones T. W., 2014, Int. J. Mod. Phys. D, 23, 1430007
Carlstrom J. E. et al., 2011, PASP, 123, 568
Cavagnolo K. W., Donahue M., Voit G. M., Sun M., 2008, ApJ, 683, L107
Cavagnolo K. W., McNamara B. R., Nulsen P. E. J., Carilli C. L., Jones C., Bîrzan L., 2010, ApJ, 720, 1066

Cavagnolo K. W., McNamara B. R., Wise M. W., Nulsen P. E. J., Brüggen M., Gitti M., Rafferty D. A., 2011, ApJ, 732, 71

Churazov E., Sazonov S., Sunyaev R., Forman W., Jones C., Böhringer H., 2005, MNRAS, 363, L91

Condon J. J., Cotton W. D., Greisen E. W., Yin Q. F., Perley R. A., Taylor G. B., Broderick J. J., 1998, AJ, 115, 1693

Daly R. A., Sprinkle T. B., O'Dea C. P., Kharb P., Baum S. A., 2012, MNRAS, 423, 2498

Danielson A. L. R., Lehmer B. D., Alexander D. M., Brandt W. N., Luo B., Miller N., Xue Y. Q., Stott J. P., 2012, MNRAS, 422, 494

Dickey J. M., Lockman F. J., 1990, ARA&A, 28, 215

Donahue M., Stocke J. T., Gioia I. M., 1992, ApJ, 385, 49

Donahue M. et al., 2010, ApJ, 715, 881

Donahue M. et al., 2015, ApJ, 805, 177

Dunlop J. S., Peacock J. A., 1990, MNRAS, 247, 19

Dunn R. J. H., Fabian A. C., 2004, MNRAS, 355, 862

Edge A. C., Stewart G. C., Fabian A. C., Arnaud K. A., 1990, MNRAS, 245, 559

Evans D. A., Worrall D. M., Hardcastle M. J., Kraft R. P., Birkinshaw M., 2006, ApJ, 642, 96

Fabian A. C., 1994, ARA&A, 32, 277

Fabian A. C., 2012, ARA&A, 50, 455

Fabian A. C. et al., 2000, MNRAS, 318, L65

Fabian A. C., Celotti A., Erlund M. C., 2006, MNRAS, 373, L16

Fabian A. C. et al., 2016, MNRAS, 461, 922

Fabian A. C., Walker S. A., Russell H. R., Pinto C., Sanders J. S., Reynolds C. S., 2017, MNRAS, 464, L1

Fanaroff B. L., Riley J. M., 1974, MNRAS, 167, 31P

Farage C. L., McGregor P. J., Dopita M. A., 2012, ApJ, 747, 28

Fernandes C. A. C. et al., 2015, MNRAS, 447, 1184

Fogarty K., Postman M., Connor T., Donahue M., Moustakas J., 2015, ApJ, 813, 117

Forman W. et al., 2005, ApJ, 635, 894

Fowler J. W. et al., 2007, Appl. Opt., 46, 3444

Gaspari M., Ruszkowski M., Sharma P., 2012, ApJ, 746, 94

Gaspari M., Ruszkowski M., Oh S. P., 2013, MNRAS, 432, 3401

Gaspari M., Brighenti F., Temi P., 2015, A&A, 579, A62

Gendre M. A., Best P. N., Wall J. V., Ker L. M., 2013, MNRAS, 430, 3086

Giacintucci S., Markevitch M., Cassano R., Venturi T., Clarke T. E., Brunetti G., 2017, ApJ, 841, 71

Gioia I. M., Henry J. P., Mullis C. R., Böhringer H., Briel U. G., Voges W., Huchra J. P., 2003, ApJS, 149, 29

Godfrey L. E. H., Shabala S. S., 2013, ApJ, 767, 12

Godfrey L. E. H., Shabala S. S., 2016, MNRAS, 456, 1172

Grimes J. A., Rawlings S., Willott C. J., 2004, MNRAS, 349, 503

Guo F., Mathews W. G., 2014, ApJ, 780, 126

Gupta N. et al., 2016, MNRAS, 467, 3737

Hall P. B., Green R. F., 1998, ApJ, 507, 558

Hardcastle M. J., Evans D. A., Croston J. H., 2006, MNRAS, 370, 1893

Hardcastle M. J., Evans D. A., Croston J. H., 2007, MNRAS, 376, 1849

Hasselfield M. et al., 2013, J. Cosmol. Astropart. Phys., 7, 008

Heckman T. M., Best P. N., 2014, ARA&A, 52, 589

Helfand D. J., White R. L., Becker R. H., 2015, ApJ, 801, 26

Hicks A. K., Mushotzky R., Donahue M., 2010, ApJ, 719, 1844

Hill G. J., Lilly S. J., 1991, ApJ, 367, 1

Hillel S., Soker N., 2014, MNRAS, 445, 4161

Hillel S., Soker N., 2017, MNRAS, 466, L39

Hilton M. et al., 2013, MNRAS, 435, 3469

Hine R. G., Longair M. S., 1979, MNRAS, 188, 111

Hlavacek-Larrondo J., Fabian A. C., Edge A. C., Ebeling H., Sanders J. S., Hogan M. T., Taylor G. B., 2012, MNRAS, 421, 1360

Hlavacek-Larrondo J., Fabian A. C., Edge A. C., Ebeling H., Allen S. W., Sanders J. S., Taylor G. B., 2013, MNRAS, 431, 1638

Hlavacek-Larrondo J. et al., 2015, ApJ, 805, 35

Ineson J., Croston J. H., Hardcastle M. J., Mingo B., 2017, MNRAS, 467, 2586

Intema H. T., 2014, SPAM: Source Peeling and Atmospheric Modelling, Astrophysics Source Code Library, record ascl:1408.006

Intema H. T., van der Tol S., Cotton W. D., Cohen A. S., van Bemmel I. M., Röttgering H. J. A., 2009, A&A, 501, 1185

Kaiser C. R., Alexander P., 1997, MNRAS, 286, 215

Kale R., Venturi T., Giacintucci S., Dallacasa D., Cassano R., Brunetti G., Macario G., Athreya R., 2013, A&A, 557, A99

Kaviraj S., Shabala S. S., Deller A. T., Middelberg E., 2015, MNRAS, 452, 774

Kirkpatrick C. C., McNamara B. R., Cavagnolo K. W., 2011, ApJ, 731, L23

Koekemoer A. M., O'Dea C. P., Sarazin C. L., McNamara B. R., Donahue M., Voit G. M., Baum S. A., Gallimore J. F., 1999, ApJ, 525, 621

Kokotanekov G. et al., 2017, preprint (arXiv:1706.00225)

Kormendy J., Ho L. C., 2013, ARA&A, 51, 511

Ledlow M. J., Owen F. N., 1996, AJ, 112, 9

Lehmer B. D. et al., 2007, ApJ, 657, 681

Li Y., Bryan G. L., Ruszkowski M., Voit G. M., O'Shea B. W., Donahue M., 2015, ApJ, 811, 73

Lin H. W., McDonald M., Benson B., Miller E., 2015, ApJ, 802, 34

Lindner R. R. et al., 2014, ApJ, 786, 49

Luo Q., Sadler E. M., 2010, ApJ, 713, 398

Ma C.-J., McNamara B. R., Nulsen P. E. J., 2013, ApJ, 763, 63

Mandelbaum R., Li C., Kauffmann G., White S. D. M., 2009, MNRAS, 393, 377

Marriage T. A. et al., 2011, ApJ, 737, 61

Mauch T., Sadler E. M., 2007, MNRAS, 375, 931

Mauch T., Murphy T., Buttery H. J., Curran J., Hunstead R. W., Piestrzynski B., Robertson J. G., Sadler E. M., 2003, MNRAS, 342, 1117

McCourt M., Sharma P., Quataert E., Parrish I. J., 2012, MNRAS, 419, 3319

McDonald M., Veilleux S., Rupke D. S. N., Mushotzky R., 2010, ApJ, 721, 1262

McDonald M., Veilleux S., Rupke D. S. N., Mushotzky R., Reynolds C., 2011, ApJ, 734, 95

McDonald M., Benson B., Veilleux S., Bautz M. W., Reichardt C. L., 2013a, ApJ, 765, L37

McDonald M. et al., 2013b, ApJ, 774, 23

McDonald M. et al., 2015, ApJ, 811, 111

McDonald M. et al., 2016, ApJ, 817, 86

McDonald M. et al., 2017, ApJ, 843, 28

McLeod B. et al., 2015, PASP, 127, 366

McNamara B. R., O'Connell R. W., 1989, AJ, 98, 2018

McNamara B. R. et al., 2000, ApJ, 534, L135

McNamara B. R., Wise M. W., Murray S. S., 2004, ApJ, 601, 173

McNamara B. R., Nulsen P. E. J., Wise M. W., Rafferty D. A., Carilli C., Sarazin C. L., Blanton E. L., 2005, Nature, 433, 45

McNamara B. R. et al., 2014, ApJ, 785, 44

McNamara B. R., Russell H. R., Nulsen P. E. J., Hogan M. T., Fabian A. C., Pulido F., Edge A. C., 2016, ApJ, 830, 79

Mernier F. et al., 2017, A&A, 603, 80

Mingo B., Hardcastle M. J., Croston J. H., Dicken D., Evans D. A., Morganti R., Tadhunter C., 2014, MNRAS, 440, 269

Mittal R., Hudson D. S., Reiprich T. H., Clarke T., 2009, A&A, 501, 835

Mittal R., Whelan J. T., Combes F., 2015, MNRAS, 450, 2564

Motl P. M., Hallman E. J., Burns J. O., Norman M. L., 2005, ApJ, 623, L63

Nulsen P., Jones C., Forman W., Churazov E., McNamara B., David L., Murray S., 2009, in Heinz S., Wilcots E. eds, AIP Conf. Ser. Vol. 1201, The Monster's Fiery Breath: Feedback in Galaxies, Groups, and Clusters. Am. Inst. Phys., New York, p. 198

O'Dea C. P. et al., 2008, ApJ, 681, 1035

O'Sullivan E., Giacintucci S., David L. P., Gitti M., Vrtilek J. M., Raychaudhury S., Ponman T. J., 2011, ApJ, 735, 11

Oonk J. B. R., Hatch N. A., Jaffe W., Bremer M. N., van Weeren R. J., 2011, MNRAS, 414, 2309

Owen F. N., White R. A., 1991, MNRAS, 249, 164

Panagoulia E. K., Fabian A. C., Sanders J. S., 2014a, MNRAS, 438, 2341

Panagoulia E. K., Fabian A. C., Sanders J. S., Hlavacek-Larrondo J., 2014b, MNRAS, 444, 1236

Peterson J. R. et al., 2001, A&A, 365, L104

Pfrommer C., 2013, ApJ, 779, 10

Pizzolato F., Soker N., 2005, ApJ, 632, 821

Pizzolato F., Soker N., 2010, MNRAS, 408, 961

Planck Collaboration XXIX, 2014, A&A, 571, A29

Pracy M. B. et al., 2016, MNRAS, 460, 2

Prasad D., Sharma P., Babul A., 2015, ApJ, 811, 108

Pratt G. W., Croston J. H., Arnaud M., Böhringer H., 2009, A&A, 498, 361

Rafferty D. A., McNamara B. R., Nulsen P. E. J., Wise M. W., 2006, ApJ, 652, 216

Rafferty D. A., McNamara B. R., Nulsen P. E. J., 2008, ApJ, 687, 899

Ramos Almeida C. et al., 2012, MNRAS, 419, 687

Reichardt C. L. et al., 2013, ApJ, 763, 127

Reiprich T. H., Böhringer H., 2002, ApJ, 567, 716

Ruel J. et al., 2014, ApJ, 792, 45

Russell H. R., McNamara B. R., Edge A. C., Hogan M. T., Main R. A., Vantyghem A. N., 2013, MNRAS, 432, 530

Russell H. R. et al., 2016, ApJ, 836, 130

Ruszkowski M., Yang H.-Y. K., Reynolds C. S., 2017, preprint, (arXiv:1701.07441)

Sadler E. M. et al., 2002, MNRAS, 329, 227

Sadler E. M. et al., 2007, MNRAS, 381, 211

Sadler E. M., Ekers R. D., Mahony E. K., Mauch T., Murphy T., 2014, MNRAS, 438, 796

Samuele R., McNamara B. R., Vikhlinin A., Mullis C. R., 2011, ApJ, 731, 31

Santos J. S., Tozzi P., Rosati P., Böhringer H., 2010, A&A, 521, A64

Shabala S. S., Deller A., Kaviraj S., Middelberg E., Turner R. J., Ting Y. S., Allison J. R., Davis T. A., 2017, MNRAS, 464, 4706

Sharma P., McCourt M., Quataert E., Parrish I. J., 2012, MNRAS, 420, 3174

Sifón C. et al., 2013, ApJ, 772, 25

Silk J., Rees M. J., 1998, A&A, 331, L1

Simionescu A., Werner N., Finoguenov A., Böhringer H., Brüggen M., 2008, A&A, 482, 97

Simpson C., Westoby P., Arumugam V., Ivison R., Hartley W., Almaini O., 2013, MNRAS, 433, 2647

Smith R. K., Brickhouse N. S., Liedahl D. A., Raymond J. C., 2001, ApJ, 556, L91

Smolčić V. et al., 2009, ApJ, 696, 24

Soker N., 2006, New Astron., 12, 38

Song J. et al., 2012, ApJ, 761, 22

Sun M., 2009, ApJ, 704, 1586

Sun M., Jones C., Forman W., Vikhlinin A., Donahue M., Voit M., 2007, ApJ, 657, 197

Tang X., Churazov E., 2017, MNRAS, 468, 3516

Tremblay G. R. et al., 2015, MNRAS, 451, 3768

Tremblay G. R. et al., 2016, Nature, 534, 218

Turner R. J., Shabala S. S., 2015, ApJ, 806, 59

Valentini M., Brighenti F., 2015, MNRAS, 448, 1979

Vantyghem A. N. et al., 2016, ApJ, 832, 148

van Weeren R. J. et al., 2014, ApJ, 786, L17

Vikhlinin A., Burenin R., Forman W. R., Jones C., Hornstrup A., Murray S. S., Quintana H., 2007, in Böhringer H., Pratt G. W., Finoguenov A., Schuecker P., eds, Heating versus Cooling in Galaxies and Clusters of Galaxies. Springer-Verlag, Berlin, Heidelberg, p. 48

Voit G. M., Donahue M., 2015, ApJ, 799, L1

Voit G. M., Cavagnolo K. W., Donahue M., Rafferty D. A., McNamara B. R., Nulsen P. E. J., 2008, ApJ, 681, L5

Voit G. M., Donahue M., Bryan G. L., McDonald M., 2015, Nature, 519, 203

Voit G. M., Meece G., Li Y., O'Shea B. W., Bryan G. L., Donahue M., 2016, preprint (arXiv:1607.02212)

Wagh B., Sharma P., McCourt M., 2014, MNRAS, 439, 2822

Werner N. et al., 2010, MNRAS, 407, 2063

Werner N. et al., 2011, MNRAS, 415, 3369

Werner N. et al., 2014, MNRAS, 439, 2291

Willott C. J., Rawlings S., Blundell K. M., Lacy M., 1999, MNRAS, 309, 1017

Willott C. J., Rawlings S., Blundell K. M., Lacy M., Eales S. A., 2001, MNRAS, 322, 536

Wylezalek D. et al., 2013, ApJ, 769, 79

Yang H.-Y. K., Reynolds C. S., 2016, ApJ, 829, 90

Yates M. G., Miller L., Peacock J. A., 1989, MNRAS, 240, 129

Yee H. K. C., Green R. F., 1987, ApJ, 319, 28

Yuan Z. S., Han J. L., Wen Z. L., 2016, MNRAS, 460, 3669

Zhuravleva I. et al., 2014, Nature, 515, 85

Zhuravleva I. et al., 2016, MNRAS, 458, 2902

This paper has been typeset from a TEX/LATEX file prepared by the author.